OXFORD GENETICS

GENETICS, 2023, 225(4), iyad184
https://doi.org/10.1093/genetics/iyad184
Advance Access Publication Date: 7 October 2023
Investigation

Adhesion and Polarity protein distribution-regulates hexagon dominated plasma membrane organization in *Drosophila* blastoderm embryos

Bipasha Dey,[1,2,†] Debasmita Mitra,[1,†] Tirthasree Das,[1,3] Aparna Sherlekar,[1,4] Ramya Balaji,[1,5] Richa Rikhy[1,*]

[1]Biology, Indian Institute of Science Education and Research, Homi Bhabha Road, Pashan, Pune 411008, India
[2]Present address: Biosystems Dynamics Research Center, Riken, Kobe 650-0047, Japan
[3]Present address: Department of Ophthalmology, University of California San Francisco, San Francisco, CA 94115, USA
[4]Present address: Department of Molecular and Cellular Physiology, Stanford University School of Medicine, Stanford, CA 94305, USA
[5]Present address: Biology, Hilde-Mangold-Haus, University of Freiburg, Freiburg, Germany

*Corresponding author: Biology, Indian Institute of Science Education and Research, Dr. Homi Bhabha Road, Pashan, Pune 411008, India. Email: richa@iiserpune.ac.in
[†]Equal contribution.

Epithelial cells contain polarity complexes on the lateral membrane and are organized in a hexagon-dominated polygonal array. The mechanisms regulating the organization of polygonal architecture in metazoan embryogenesis are not completely understood. *Drosophila* embryogenesis enables mechanistic analysis of epithelial polarity formation and its impact on polygonal organization. The plasma membrane (PM) of syncytial *Drosophila* blastoderm embryos is organized as a polygonal array with pseudocleavage furrow formation during the almost synchronous cortical division cycles. We find that polygonal (PM) organization arises in the metaphase (MP) of division cycle 11, and hexagon dominance occurs with an increase in furrow length in the metaphase of cycle 12. There is a decrease in cell shape index in metaphase from cycles 11 to 13. This coincides with *Drosophila* E-cad (DE-cadherin) and Bazooka enrichment at the edges and the septin, Peanut at the vertices of the furrow. We further assess the role of polarity and adhesion proteins in pseudocleavage furrow formation and its organization as a polygonal array. We find that DE-cadherin depletion leads to decreased furrow length, loss of hexagon dominance, and increased cell shape index. Bazooka and Peanut depletion lead to decreased furrow length, delay in onset of hexagon dominance from cycle 12 to 13, and increased cell shape index. Hexagon dominance occurs with an increase in furrow length in cycle 13 and increased DE-cadherin, possibly due to the inhibition of endocytosis. We conclude that polarity protein recruitment and regulation of endocytic pathways enable pseudocleavage furrow stability and the formation of a hexagon-dominated polygon array.

Keywords: syncytium; embryo; epithelia; polygon; *Drosophila*; DE-cadherin; Bazooka; septin

Introduction

Epithelial tissues consist of adherent cells that line the internal and external surfaces of various metazoans. These cells are classified by the presence of 3 major hallmark features. First, epithelial cells show the asymmetric distribution of polarity protein complexes on the plasma membrane (PM), thereby dividing it into the apical, lateral, and basal domains. These polarity complexes are important for cell shape, tissue integrity, and tissue remodeling (Bilder et al. 2000; Hayashi and Carthew 2004; Letizia et al. 2013; Laprise and Tepass 2011). Second, epithelial cells adhere to each other via junctional complexes that enable them to form a leak-proof sheet that functions as a barrier to seal off either an organism's or an organ's interior from the external environment. Third, epithelial tissues across metazoans exhibit a polygonal cell shape distribution with a predominance of hexagonal shapes. Though the functional and molecular details of polarity and junctions in epithelia have been extensively laid out, their role in regulating hexagon dominance is not fully understood.

Hexagon dominance is a conserved property of epithelia seen in organisms ranging from the diploblastic *Hydra* to the triploblastic *Xenopus* (Gibson et al. 2006; Farhadifar et al. 2007) and, in some cases, exhibits dynamic evolution over developmental stages (Classen et al. 2005; Sánchez-Gutiérrez et al. 2013). One of the fundamental ideas in theoretical studies is that hexagon dominance results simply from surface energy minimization. Similar to the arrangement of soap bubbles being driven by surface tension, epithelial cells organize into a polygonal array by maximizing the cell area in contact with the neighbors while minimizing the surface area exposed to the environment. Additionally, asynchronous divisions, cell mechanical properties defined by adhesion and contractility, cellular rearrangements as well as global tissue level forces have also been implicated in regulating this distribution (Gibson et al. 2006; Farhadifar et al. 2007; Aegerter-Wilmsen et al. 2010; Sugimura and Ishihara 2013). On the other hand, molecular factors that facilitate this energy-minimized organization are just beginning to be explored. For example, lowered *Drosophila* E-cad (DE-cad) turnover in endocytic mutants results in a decrease

Received on 29 August 2023; accepted on 25 September 2023

in the frequency of hexagons in *Drosophila* wing discs. DE-cad recycling is, in turn, regulated by planar cell polarity (PCP) proteins, therefore, an interplay of adhesion and PCP proteins regulates the frequency of hexagons in wing disc epithelium (Classen et al. 2005; Iyer et al. 2019). In human keratinocytes, loss of MyosinII activity in ROCK1 and ROCK2 mutants also results in a low percentage of hexagonally shaped cells (Kalaji et al. 2012). Cell shape index, which is a measure of jammed epithelia, increases with the onset of germ band extension on the increase of elongated and pentagonal cells (Wang et al. 2020). These examples corroborate the theoretical studies suggesting that molecules regulating adhesion, contractility, and polarity could be important determinants of hexagon dominance. However, how the temporal onset of polarity correlates with the onset of hexagon dominance in epithelia is not well understood.

Metazoan embryogenesis shows the onset of epithelial-like polarity and formation of a polygonal array and, therefore, provides the opportunity to address the mechanisms that regulate the onset of hexagon dominance (Nance 2014). An analysis of the onset of polygonal PM packing and the factors that determine this in embryogenesis has not been characterized thus far. In this study, we use the syncytial *Drosophila* blastoderm embryo to characterize the temporal onset of polygonal packing and the role of polarity and adhesion proteins in regulating its dynamics. *Drosophila* embryogenesis begins with nuclear division cycles (NC) 1–8 occurring deep in the interior of the embryo followed by nuclear migration to the cortex during NC9 (Foe and Alberts 1983; Miller et al. 1985). The arrival of the nuclei can be seen as buds called caps at the cortex (Foe and Alberts 1983; Miller et al. 1985). The NCs10–14 occur in an almost synchronous manner near the cortex without undergoing complete cytokinesis, thereby, resulting in the formation of a syncytial blastoderm. The PM is organized as circular caps in the interphase and converts to a polygonal array with furrow extension, showing a cyclical behavior of circular to polygonal transition during each syncytial division cycle (Dey and Rikhy 2020). Cytoskeletal and PM dynamics help maintain a hexagon-dominated polygonal arrangement of nuclei during these syncytial cycles (Kanesaki et al. 2011; Kaiser et al. 2018; Lv et al. 2020).

The syncytial blastoderm embryo shows the asymmetric distribution of various polarity and cytoskeletal proteins on the PM (Schmidt and Grosshans 2018). To begin with, the *Drosophila* embryo is cortically uniform at the preblastoderm stage. The first cortical differentiation occurs during NC10 where the cortex is divided into 2 domains during interphase; the cap and intercap regions. The cap region is enriched in F-actin and actin-associated proteins such as Arp2/3, SCAR, Moesin, ELMO, Sponge, and α-spectrin, while the intercap region is marked by Myosin II, Toll and Slam. The PM begins to be organized into a polygonal array with furrow extension during syncytial division cycles 11 to 14. Particularly at metaphase (MP), the PM is segregated into 3 domains; apical, lateral, and basal domain. In the syncytial system, the basal domain refers to the tip of the pseudocleavage furrow. The lateral region is occupied by Canoe, Peanut (Pnut), Scrambled, DE-cad, Bazooka (Baz), Dlg, and Toll; and the furrow tip shows enrichment of PatJ, Amphiphysin, Anilin, Diaphanous, and Syndapin (Pesacreta et al. 1989; Thomas and Williams 1999; Foe et al. 2000; Stevenson et al. 2002; Zallen et al. 2002; Mavrakis et al. 2009; Rikhy et al. 2015; Sherlekar and Rikhy 2016; Schmidt et al. 2018; Schmidt and Grosshans 2018; Dey and Rikhy 2020). Therefore, the syncytial *Drosophila* blastoderm embryo shows molecular and morphological asymmetries in the PM along with the formation of a polygonal array at MP during the syncytial cycles. However, how these asymmetries impact the onset, distribution, and dynamics of the polygonal array remains to be investigated.

In our previous study, we showed that the extension of the furrow in between adjacent nuclei leads to the onset of polygonal organization in syncytial division cycles 11 to 14 (Dey and Rikhy 2020; Sherlekar et al. 2020). In this study, we assess the role of polarity and adhesion proteins in regulating the polygonal PM organization on the increase in furrow extension and in MP of the cortical syncytial cycles. We find that the PM of the embryo is organized as a hexagon-dominated polygonal array for the first time in NC12 at the final furrow length achieved at MP. There is a decrease in the anisotropy of shapes and cell shape index with the progression of the syncytial division cycles. DE-cad and Baz are enriched at the edges while Peanut is enriched at the vertices in these polygonal cells. DE-cad depletion leads to a short furrow, loss of hexagon dominance, and an increase in cell shape index. Baz and Pnut depletion also leads to a minor decrease in furrow length, an increase in cell shape index, and a delay in hexagon dominance when the furrow length increases in NC13. This is accompanied by the accumulation of key endocytic proteins and DE-cad at the furrow.

Materials and methods

Fly stocks, crosses, and lethality estimation

Drosophila melanogaster stocks were raised in standard cornmeal agar at 25°C and 29°C for RNAi experiments. Embryos obtained from CantonS flies or CantonS flies crossed to *maternal α-tubulin* Gal4-VP16 (*mat*-Gal4) or *nanos*-Gal4 (*nos*-Gal4) were used as control. The information on fly genes and stocks was obtained from Flybase (Gramates et al. 2022). Maternal driver line *mat67; mat15* carrying *maternal α4 tubulin*-Gal4-*VP16* (obtained from Girish Ratnaparkhi, IISER, Pune, India), homozygous for chromosome II and III was used for all RNAi and overexpression experiments except for shg^{i} for which *nos*-Gal4 was used. Baz RNAi (Bloomington Stock number #35002), Pnut RNAi (#65157), DE-cad RNAi (#38207), tGPH (#8163), UASp-Baz-GFP (#65845), endo-DE-cad-GFP (#60584), and baz^{G0484} lines were obtained from the Bloomington Stock Center, Indiana, Bloomington, USA. ubi-cad-GFP was obtained from the Maithreyi Narasimha lab from TIFR, Mumbai, India. $pnut^{XP}$ FRTG13/CyO and *UASp*-Pnut-mCherry stocks were obtained from Manos Mavrakis, Fresnel University, Marseilles, France. Baz truncation domain constructs were obtained from Andreas Wodarz, Goettingen University, Germany. *Sqh*-Sqh Cherry, *mat67*-Gal4; *ubi*-DE-cad-GFP, *mat15*-Gal4/TM3Sb was obtained from Adam Martin's lab, MIT, Massachusettes, USA. *Sqh*-Sqh GFP, *mat67*-Gal4 from Thomas Lecuit, IBDM, Marseilles, France.

F1 flies were put in a cage for egg collection to perform immunostaining or live imaging. Germline clones of $pnut^{XP}$ were made by crossing ovo^{D} FRTG13 males to *hsflp; GlaBlc* females to obtain hsflp; ovo^{D} FRTG13/*GlaBlc* males. These males were then crossed to $pnut^{XP}$ FRTG13/*Cyo* females. Larvae, pupae, and adults emerging from this cross were heat-shocked at 37.5°C. hsflp; ovo^{D} FRTG13/$pnut^{XP}$ FRTG13 adults were then put in a cage to collect embryos depleted of *pnut*. shg^{i} was crossed to a single chromosomal copy of *nos*-Gal4 and maintained at 18°C to lower the severity of phenotype and obtain fertilized eggs to perform experiments. F1 flies expressing shg^{i} with *nos*-Gal4 when grown at 25 or 29°C, laid embryos that were arrested early in the pre-blastoderm stage of development and, hence, the experiments were performed at 18°C to allow for Gal4 dilution. This cross at 18°C gave enough embryos that entered the syncytial cycles. The lethality of shg^{i} embryos

was 100% ($n = 150$) at 25°C and 29°C and 70% ($n = 200$) at 18°C after 24 hrs. The lethality of *pnut*^{i} and *baz*^{i} expressing embryos and *pnut*^{XP} germline clones was 100% ($n = 300$ embryos each).

Immunostaining

0–2.5 hr old embryos were collected on sucrose agar plates, washed, and dechorionated with 100% bleach for 1 min. Embryos were fixed using a 1:1 mixture of 4% paraformaldehyde in PBS and Heptane for 20 min. Fixed embryos were either hand-de-vitellinized for phalloidin staining or MeOH de-vitellinized, washed thrice in 1× PBST (1× PBS with 0.3% Triton ×100), and blocked in 2% BSA (Sigma-Aldrich, India) in 1× PBST for 1 hr. Primary antibody was then added at an appropriate dilution and incubated overnight, followed by 3 1× PBST washes, and 1 hr incubation in appropriate fluorescently coupled secondary antibodies at 1:1000 (Molecular probes, Bangalore, India). Hoechst 33,258 was added for 10 min in 1× PBST. Finally, the embryos were washed 3 times in 1× PBST and mounted in Slow fade Gold antifade reagent (Molecular Probes). The primary antibodies used were: rabbit anti-Baz (1:1000 from Andreas Wodarz, Germany), mouse anti-Pnut (1:5, DSHB), mouse anti-Dlg (1:100 DSHB), rabbit anti-Patj (1:1000 from Hugo Bellen, USA), rat Sep1 (1:250 from Manos Mavrakis, France), guinea pig Sep2 (1:250 from Manos Mavrakis, France), rat anti-DE-cad (1:5, DSHB), guinea pig anti-Rab5 (1:500 from Akira Nakamura, Japan) (Tanaka et al. 2021), mouse anti-Dynamin (1:200 BD Transduction Laboratories). DNA was stained with Hoechst 33258 (1:1000, Molecular Probes, Bangalore, India).

Live imaging of *Drosophila* embryos

1–1.5 hr old embryos expressing the membrane marker tGPH or Sqh-GFP or Sqh-mCherry; DE-cad-GFP were collected and dechorionated with 100% bleach for 1 min and mounted on coverslip-bottomed LabTek chambers (Mavrakis et al. 2008). The chambers were then filled with 1× PBS and imaged on Zeiss Plan Apochromat 40X/1.4 NA oil objective.

Microscopy

Live or fixed embryos were imaged on any of the following laser scanning confocal microscopes: Zeiss LSM710, LSM780, and Leica SP8. The 40× objective with NA 1.4 was used to image living and fixed embryos. The Argon laser was used to image GFP in tGPH, DE-cad-GFP, Baz-GFP, and Sqh-GFP. The Diode 561 laser was used to image the Sqh-mCherry and Pnut-mCherry. Care was taken to maintain the laser power and gain with the range indicator mode such that the 8-bit image acquired did not show any saturation and was within the 0–255 range. Averaging of 2 was used for both fixed and live imaging. Images were acquired with an optical section of 1.08 microns in all except F-actin stainings, where an optical section of 0.34 microns was used.

Embryo lethality

3–4 hr old embryos were collected, washed, and arranged into a 10 × 10 matrix on a sugar-agar plate using a brush. The number of unhatched embryos was counted after 24 hrs. This procedure was repeated 3 times for each genotype tested.

Quantification and statistical analysis

Image quantification

Polygon analysis. The most taut and bright grazing section from MP (usually at the base of the furrow) of each NC per embryo was used to quantify polygons using the Packing analyzer software (Benoit Aigouy, Classen et al. 2005). The software allows the segmentation of the PM surrounding each cell (Fig. 1a). Note that the segmented edges have curved edges similar to the actual images. The cell area and perimeter are estimated from each cell in the rendered image. The image is color-coded according to polygon type. It is important to note that represented color-coded polygon-rendered images contain straight edges. The output is available in an Excel sheet with the area, perimeter, and polygon type of each cell in the field. Three or more embryos were used per NC and all the cells in the field were analyzed this way to obtain the polygon distribution per cycle.

Quantification of cell shape index

Based on the cell segmentation data obtained from the Packing analyzer software (Fig. 1a) and from the area (A) and perimeter (P) data obtained as an output, cell shape index was calculated using the formula: $P/\sqrt{A}$ (Bi et al. 2015). It is important to note that the cell shape index is estimated from the segmented images and not the color-coded images used to document the polygon distribution shown in each figure. Three or more embryos were used for each NC and all the cells in the field were analyzed to calculate the average cell shape index.

Quantification of relative fluorescent signal across the depth and in planar sections of the plasma membrane

The grazing sections at MP across depth expressing various polarity proteins were used for this analysis. A region of interest (ROI) was drawn at 5 edges and 5 vertices for MP11, and 10 edges and 10 vertices for MP12-13, in each optical section from apical to basal sections. Optical sections were taken at approximately 1 µm depth across the entire furrow. The mean intensities from these ROIs were measured using ImageJ (Schneider et al. 2012). The intensities from each stack were background subtracted. The graphs shown in Fig. 2 represent mean intensities obtained across the depth of the furrow normalized to the mean intensity of the apical-most optical section in NC11.

Quantification for Sep1 and Sep2 was done by creating 5 ROIs on the edge and the vertex as mentioned above. The mean intensities were normalized by dividing by the mean intensity of the entire field.

Enrichment in the basal furrow region and edge/vertex was computed by performing statistical analysis for the fluorescence values on the length of the furrow using 2-way ANOVA to test how the intensity of signals varied with either edge/vertex or apical/basal regions of the furrow.

The change in the fluorescence intensity at the furrow membrane was estimated at MP11, MP12, and MP13 by measuring 5 different ROIs corresponding to the furrow membrane and divided by the fluorescence in the neighboring cytosol.

Quantification of the MP furrow length

Metaphase furrow lengths were quantified from the orthogonal sections for different time points and NCs using the Zen Blue software. Five to eight furrows were measured per time point per embryo. These lengths were further confirmed with the number of z-stacks taken to cover the entire furrow length of syncytial cells in the field of view.

Quantification of fluorescence from antibody stainings

Baz, Pnut, DE-cad, Dynamin, and Rab5 antibody and DE-cad-GFP staining were quantified by estimating the fluorescence at 5

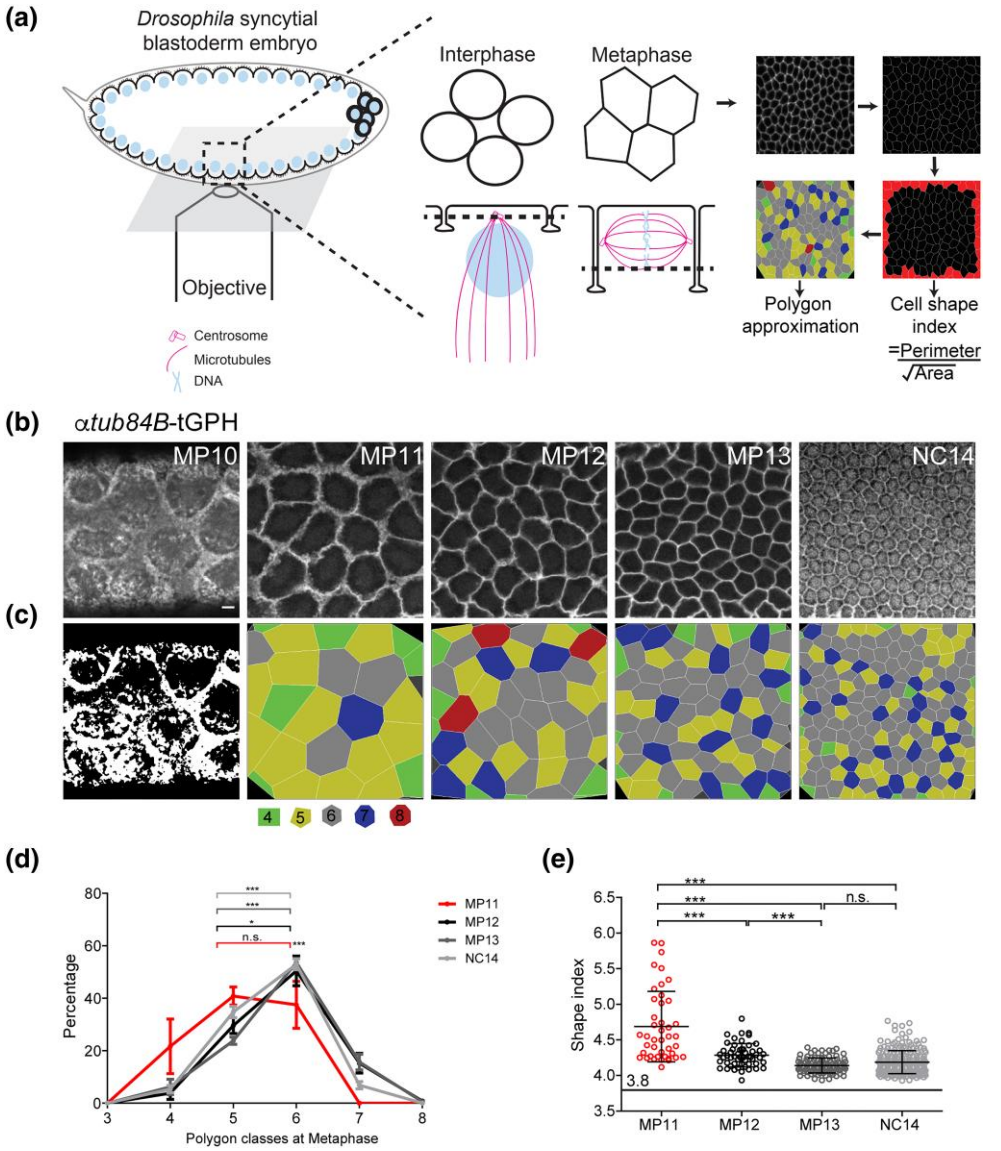

Fig. 1. Hexagon dominated PM organization emerges in NC12. Schematic showing the syncytial *Drosophila* blastoderm embryo in interphase being imaged by an objective at the bottom on an inverted confocal microscope. The zoomed inset shows sagittal and XY views of syncytial cells in both interphase and MP turned 180° with the PM at the top. XY views are the cross-sections along the MP furrow at a length represented by the dotted lines. The PM shows polygonal organization in MP. The right-hand side of the schematic shows the pipeline for image analysis. The acquired fluorescent images are segmented in packing analyzer for obtaining cell boundaries which are used to estimate the cell shape index. Note that the cells have wavy edges in the MP13 image shown. The cells at the edges are omitted for calculations. The segmented images are rendered for estimation of polygon distribution across the MP10–14. Note that the representation has straight edges rendered in the polygon distribution images (a). Grazing sections of *αtub84B*-tGPH expressing embryos from MP10–13 and NC14, tGPH labels the entire membrane in MP10–13 and enters the nucleus in NC14 in addition to being at the PM (b). Color-coded polygon rendering of the respective images in B using the packing analyzer software (c). Quantitative analysis of polygon distribution in MP11–13 and NC14 ($n = 20$–60 cells from NC11–14 per embryo, 4 embryos). Each curve represents a single NC (d). Pentagons and hexagons are compared using the unpaired, 2-tailed, Student's *t* test. Data is represented as mean ± SEM, $^{*}P < 0.05$, $^{**}P < 0.01$, and $^{***}P < 0.001$. Graph shows the average shape index of all the cells in the field for control embryos (e) ($n = 20$–60 cells from MP11–13 and NC14 per embryo, 4 embryos). Data is represented as mean ± SEM, $^{*}P < 0.05$, $^{**}P < 0.01$, and $^{***}P < 0.001$, 2-tailed, unpaired Student's *t*-test. Scale bar: 5 μm.

furrow membranes from each embryo as compared to the cytosol in controls and mutants at the same stage.

Statistical analysis

All data are represented as mean ± SD or SEM. Statistical significance was determined using the 2-tailed, unpaired, Student's *t*-test in most cases, to compare between 2 means. One-way ANOVA was used when comparing 3 or more means together, with Dunnett's Multiple Comparison Test as a post-test to compare all means to control. Student's *t*-test was used to compare hexagons to pentagons in each NC per genotype to determine hexagon dominance.

Results

Onset of hexagon-dominated plasma membrane architecture occurs during nuclear cycle 12 in syncytial *Drosophila* blastoderm embryos

To assess the syncytial NC at which optimal packing and hexagon-dominated polygon organization emerge during the syncytial

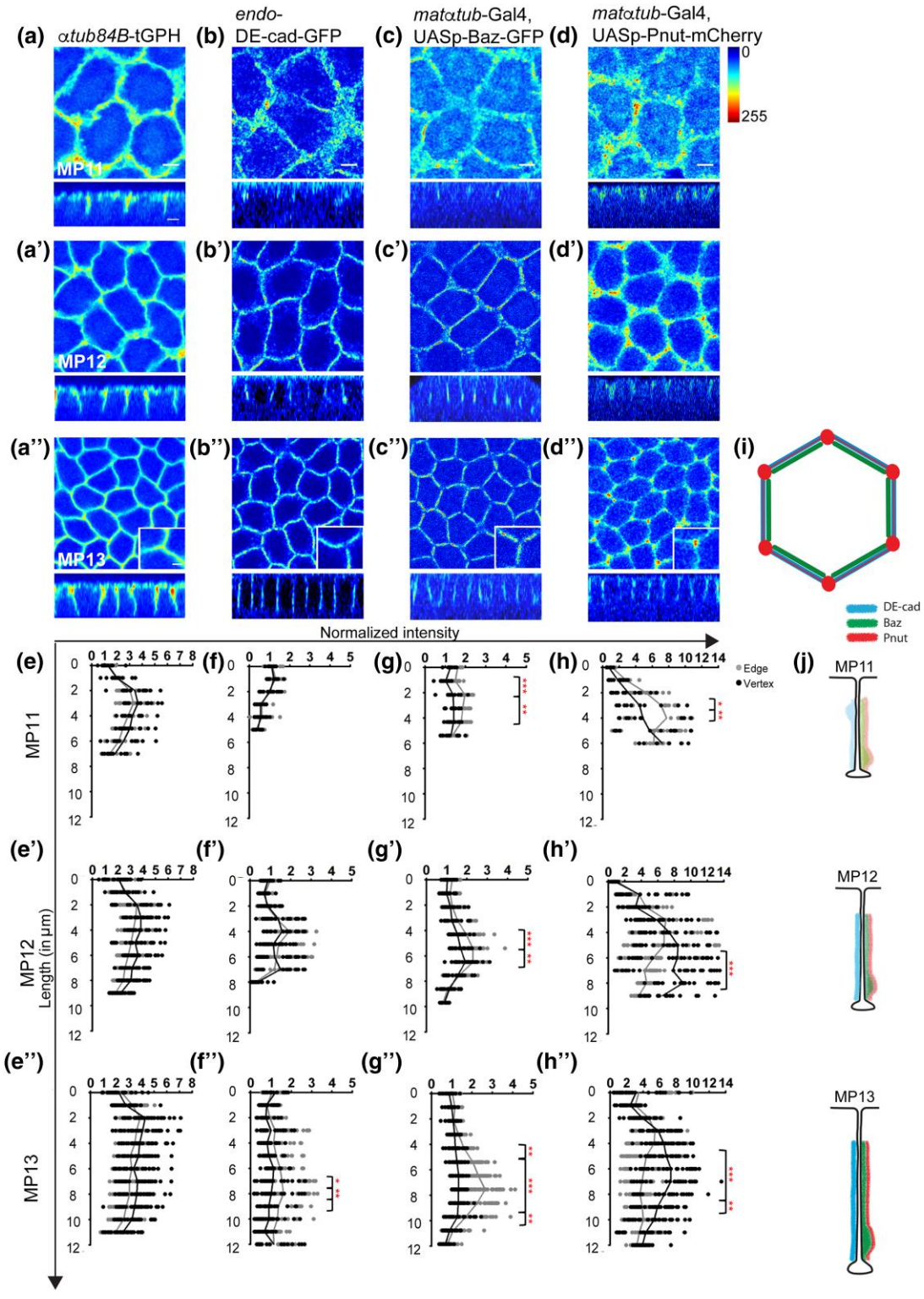

Fig. 2. DE-cad, Baz and Pnut show polarized distribution in the syncytial cells. a–b) Distribution of *atub84B*-tGPH (a: MP11, a′: MP12 and a″: MP13), *endo*-DE-cad-GFP (b: MP11, b′: MP12, and b″: MP13), *matatub*-Gal4; Baz-GFP (c: MP11, c′: MP12, and c″: MP13) and *matatub*-Gal4; Pnut-mCherry (d: MP11, d′: MP12, and d″: MP13) in grazing and sagittal views in syncytial MP11–13. The Jet rainbow scale from ImageJ is used to show fluorescent intensities. tGPH labels the entire PM, DE-cad is enriched at edges in MP13 (a″-b″ insets show zoomed-in images), Baz is enriched at edges MP11 onward while Pnut is enriched on the vertex MP12 onward (c″-d″ insets show zoomed in images). e–h) Quantification of intensities normalized to the apical section of NC11 in edges (black) and vertices (gray) along the MP furrow length for *atub84B*-tGPH (E: NC11, E′: NC12, E″: NC13), *endo*-DE-cad-GFP (F: MP11, F′: MP12, F″: MP13), *matatub*-Gal4; Baz-GFP (G: MP11, G′: MP12, G″: MP13′), and *matatub*-Gal4; Pnut-mCherry (H: MP11, H′: MP12, H″: MP13) in NC11–13 ($n = 3$ embryos each). i and j) Schematic representing the polarized localization of proteins in XZ and XY planes. Asymmetric distribution of DE-cad, Baz, and Pnut between edges and vertices in the XY plane (i). Asymmetric distribution of DE-cad, Baz, and Pnut across MP11–13 along the apico-basal axis in the XZ plane (j). While DE-cad spreads all across the length, Baz, and Pnut are enriched in the basal part of the furrow region. The scatter plots contain a line connecting the means, $^{*}P < 0.05$, $^{**}P < 0.01$, and $^{***}P < 0.001$, 2-way ANOVA with Bonferroni post-tests. The stars show significance between edge and vertex intensities at the indicated length based on the post test. Scale bar = 5 µm. The zoomed-in insets show a scale bar of 2 µm.

blastoderm development, we performed live imaging of tGPH (*atub84B*-tGPH) expressing embryos. tGPH contains the PH domain of GRP fused to GFP (GPH). The tGPH PH domain binds phospholipid PIP3 and labels the PM uniformly in the syncytial *Drosophila* embryo (Britton et al. 2002; Sherlekar and Rikhy 2016; Dey and Rikhy 2020). We used the packing analyzer software to segment the polygonal array to estimate the polygon distribution and the shape index from the MP stage of NC10, 11, 12, and 13 and in the interphase of NC14 (referred to as MP10, MP11, MP12, MP13, and NC14, respectively) (Fig. 1a). The nucleo-cytoplasmic domains seen as caps at the cortex were relatively far apart in MP10 (Fig. 1b, Supplementary Video 1). The furrow length increases during each cycle from NC11 to 13 from interphase to MP in between adjacent nucleo-cytoplasmic domains and it reaches a maximum in MP13 (Foe and Alberts 1983; Holly et al. 2015; Xie and Blankenship 2018; Dey and Rikhy 2020). During *Drosophila* embryogenesis, the PM was organized into a polygonal array for the first time in NC11 (Fig. 1b). The polygonally organized PM in MP13 and NC14 was more taut as compared to MP11 and MP12. MP11 showed almost equal numbers of pentagons and hexagons in the polygonal array. The polygonal array then became dominated by hexagons in MP12. This hexagon dominance persisted in MP13 and NC14 (Fig. 1c and d). While observing the onset of the formation of the polygonal array, we noted that edges formed before vertices in NC11 (Supplementary Fig. 1a).

A theoretical framework for confluent epithelial monolayers defines a non-dimensional parameter called the shape index estimated from the ratio of the perimeter and area of each cell as a predictor of tissue material properties (see materials and methods) (Bi et al. 2015; Park et al. 2015). Below a critical value of 3.81, the tissue becomes jammed or solid-like with cells displaying isotropic shapes and being caged within their radii (Bi et al. 2015). In *Drosophila* germ band extension, the tissue elongation phase shows an increase in anisotropic cell shapes and an increase in cell shape index along with an increase in the fraction of pentagons (Wang et al. 2020). We estimated the cell shape index in MP11, MP12, MP13, and NC14 from the perimeter and area output from segmented images from the movies of embryos expressing tGPH (Fig. 1e). First, we found that the cell shape index was greater than 3.81 in MP11, MP12, MP13, and NC14 suggesting that the syncytial epithelium at MP has a more fluid-like property. Additionally, we found that there was a decrease in the cell shape index from MP11 (average of 4.67) to MP12 (4.28) to MP13 (4.14) and NC14 (4.19). This result is consistent with the observations in a previous study in mammalian epithelial cells that show a decrease in the shape index with an increase in cell density with proliferation (Vishwakarma et al. 2020). This shows that the PM organization in the syncytial *Drosophila* embryo in MP forms a soft network that could facilitate the fast dynamics of cellular organization seen in each syncytial cycle. It also suggests that with each division cycle, the cell shapes become more isotropic and the system moves closer to a more rigid or solid-like phase.

Similar to previous studies (Holly et al. 2015; Dey and Rikhy 2020), we found that the furrow length increases across syncytial cycles 11 to 13 and was approximately 7 μm in MP11, 9 μm in MP12 and 11 μm in MP13 with tGPH. Our previous studies show that the onset of polygon architecture occurs at the furrow length of approximately 6 μm during each syncytial division (Dey and Rikhy 2020). Therefore, we analyzed the polygon distribution at a lower length of approximately 6.5 μm in NC12 and NC13 when polygonal architecture was visible across the embryo. We found that at this lower furrow length in NC12, the average number of pentagons was more than hexagons but this was not statistically significant, whereas in NC13 hexagons were dominant at 6.5 μm (Supplementary Fig. 1b–d). Therefore, hexagon dominance was first seen in NC12 at increased furrow lengths in MP (furrow length 9 μm) and hexagon dominance was already seen at the short furrow length of 6.5 μm in NC13. The cell shape index was significantly increased at 6.5 μm in the NC12 (4.38) and NC13 (4.25) as compared to the longest furrow length in MP (Supplementary Fig. 1e). Together, these data show that epithelial-like hexagon dominance first occurs in syncytial NC12 at longer furrow lengths in MP, even before complete cells are formed in the *Drosophila* blastoderm embryo. Coincident with an increase in hexagons, the cell shape index decreases indicating a more stable epithelial-like network. This organization is also consistent with the observation of nuclei present in a hexagon-dominated polygonal array shown previously (Kanesaki et al. 2011; Kaiser et al. 2018).

DE-cadherin, Bazooka, and Peanut are asymmetrically distributed along the furrow in the *Drosophila* syncytial blastoderm

Since the syncytial embryo PM was organized into an epithelial-like polygonal array starting from NC11 and became hexagon dominant during NC12 with an increase in furrow length, we tested if polarity proteins were progressively enriched in the lateral furrows from NC11 to NC13. DE-cad and Baz have been found in the syncytial furrow and form apical spot junctions in cellularization (Harris and Peifer 2004). To characterize the temporal distribution of DE-cad and Baz as compared to tGPH in NC11–13, we performed live imaging of embryos expressing DE-cad-GFP under the endogenous promoter (Huang et al. 2009) and Baz-GFP in control and mutant backgrounds with *matatub*-Gal4 (Benton and St Johnston 2003). The PM in epithelial cells shows a distinct distribution of proteins along tricellular junctions, which function in sealing the intercellular space (Schulte et al. 2003; Ikenouchi et al. 2005); as well as along the lateral domain. We quantified the intensity of the fluorescently tagged DE-cad and Baz and the PM marker tGPH in edges and vertices of the polygonal array along with different optical sections along the length of the furrow in MP11, MP12, and MP13 (Fig. 2a–c). The total intensities obtained at the furrow were plotted as a fold change with respect to the apical section of NC11 in each embryo (Fig. 2e–g). tGPH was distributed evenly across the furrow in edges and vertices and marked the entire length of the furrow in the lateral views (Fig. 2a-a″, e-e″). For DE-cad, we quantified the intensities using the DE-cad-GFP expressed at the endogenous gene location (Huang et al. 2009). We found that DE-cad was uniform across edges and vertices in MP11 and MP12 and was enriched at edges in MP13 (Fig. 2b-b″, f-f″). DE-cad was present along the entire MP furrow in MP11 and MP12, while in MP13 it was enriched in the basal part of the furrow from 7 to 10 μm (Fig. 2b-b″, f-f″). For Baz-GFP, we have expressed the GFP in the control and mutant (baz^{G0484}) background with *matatub*-Gal4 (see materials and methods, Fig. 2 and Supplementary Fig. 2). Baz-GFP was present along the entire membrane with enrichment at edges in MP12 and MP13 when present in the control and mutant background (Fig. 2c-c″, Supplementary Fig. 2e). Baz was enriched at the furrow between 2 and 5 μm in MP11 and toward the basal part of the furrow from 4 to 6 μm in MP12 and from 6 to 10 μm in MP13 (Fig. 2c-c″, g-g″).

The septin family proteins Pnut, Sep1, and Sep2 were also studied because Pnut is present at the furrow in syncytial stages and functions in actin organization and furrow extension (Silverman-Gavrila and Silverman-Gavrila 2008). Pnut-mCherry (Guillot and Lecuit 2013) expressed in control embryos was used

to assess the distribution of Pnut on the membrane in edges and vertices and along the length of the furrow across the syncytial cycles. Pnut was present throughout the membrane and was enriched at vertices in MP11. Pnut was concentrated toward the basal part of the furrow at 5–8 μm in MP12 and 5–10 μm in MP13 (Fig. 2d-d″, h-h″). Vertex enrichment was also observed for Sep1 and Sep2 using Sep1-GFP, Sep2-GFP (Supplementary Fig. 2a–d). Immunostainings against endogenous Sep1 and Sep2 showed an increase at vertices (Supplementary Fig. 2a–d). Pnut was also found to be enriched at vertices in immunostainings against the endogenous protein (Supplementary Fig. 3a).

We estimated the fold change of total DE-cad, Baz, and Pnut fluorescence on the PM across the syncytial cycles as compared to MP11 (Supplementary Fig. 2e and f). We found that DE-cad successively increased from MP11 to MP12 to MP13 (Supplementary Fig. 2f). Pnut-mCherry was present at a significantly higher intensity on the furrow membrane in MP13 as compared to MP11 and MP12 (Supplementary Fig. 2f). Baz was present at a higher intensity in NC12 as compared to NC11 when Baz-GFP was expressed in the control and mutant background. Baz did not change significantly from MP12 to MP13 in both the control and the *baz*^{G0484} mutant background (Supplementary Fig. 2f). This progressive increase in the distribution of DE-cad, Baz, and Pnut across the syncytial cycles implied a function of these proteins in the formation and stabilization of furrows along with polygonal architecture. The syncytial PM showed asymmetries in the planar axis of the polygon at edges (DE-cad, Baz) and vertices (Pnut) and enrichment of proteins along the base of lateral furrow from MP12 to MP13 (Fig. 2i and j).

DE-cad regulates both Baz and Pnut distribution and Baz regulates Pnut distribution at the syncytial furrow membrane

Since polarity proteins are known to regulate cell shape and hexagon dominance, we dissected the role of DE-cad, Baz, and Pnut on furrow formation and hexagon dominance. We first investigated their loss-of-function effects on the distribution of the polarity proteins in the syncytial cycles. We assessed the role of DE-cad in the recruitment of Baz and Pnut by maternally expressing DE-cad RNAi (*shg*^{i}). Similar to our previous studies, DE-cad depletion showed a decrease in DE-cad immunostaining as compared to controls (Fig. 3a) (Dey and Rikhy 2020). DE-cad-depleted embryos also showed a significant decrease in the localization of Baz and Pnut on the syncytial furrows and an increase in their cytoplasmic distribution (Fig. 3b–d). The enrichment of Pnut at vertices as compared to controls was not seen upon DE-cad depletion (Fig. 3b).

Next, we assessed the role of Baz on Pnut distribution by maternally expressing *baz* RNAi (*baz*^{i}) (see *Material and methods* for details). Baz protein levels as assessed by an antibody against the N-terminus of the protein (Wodarz et al. 1999) were lower in these embryos as compared to controls (Fig. 3e and f). Interestingly, with the knockdown of Baz, Pnut was also lowered (Fig. 3e and g) suggesting a possible role of Baz in the stabilization of Pnut on the membrane. To determine the effect of the loss of Pnut on Baz and Pnut localization, we generated germline clone embryos of null mutants of Pnut (*pnut*^{XP}) (Neufeld and Rubin 1994). *pnut*^{XP} embryos showed a significant reduction of Pnut while Baz localization remained unaffected (Fig. 3e–g). Thus, the presence of Pnut was not important for Baz localization on the syncytial PM.

To further verify if Pnut localization depended on Baz association with the syncytial PM, we maternally overexpressed truncated transgenes of Baz containing the N terminus oligomerization domain or the C terminus phospholipid membrane-binding domain fused to GFP. A GFP-tagged C-terminal truncation mutant of Baz, BazΔ969-1464-GFP, which is defective in PM recruitment (Krahn et al. 2010) was expressed maternally in the presence of wild-type protein. The GFP fluorescence pattern could be used to ascertain the distribution of the truncated transgene and the antibody against the N terminus could be used to identify the distribution of the total Baz protein. BazΔ969-1464-GFP showed a cytosolic pattern in the MP stage of NC13 showing that the C terminal truncation leads to loss of association with the furrow. Baz antibody staining against the N-terminus of the protein also showed an increased cytosolic distribution and a diffused membrane localization as compared to controls (Supplementary Fig. 3a and b). Since Baz forms oligomers in vivo (Benton and St Johnston 2003), we speculate that the N-terminal domain oligomerizes in this overexpression mutant, leading to the reduction of Baz from PM and an increase in the cytosol, in addition to the attenuated levels of Pnut. On the other hand, when a GFP-tagged Baz N-terminal truncation mutant, BazΔ1-904-GFP was maternally overexpressed, both the truncated and endogenous Baz could localize on the membrane. Pnut distribution was weaker than that seen in controls but it was present on the membrane (Supplementary Fig. 3a and c). Thus, the C-terminal domain of Baz was important not only for its own recruitment on the PM but also for Pnut membrane localization.

In summary, these observations show that DE-cad regulates the recruitment of Baz and Pnut, and Baz, in turn, regulates the distribution of Pnut on the syncytial furrow.

DE-cad, Baz, and Pnut-depleted embryos show decreased furrow length and skewed polygon distributions

So far we found that DE-cad, Baz, and Pnut distributed asymmetrically on the syncytial furrow PM (Fig. 2). Further, DE-cad depletion led to decreased levels of Pnut and Baz, while Baz depletion reduced the levels of Pnut on the syncytial furrow (Fig. 3). Previous reports show that DE-cad and Pnut loss leads to shorter MP furrows (Silverman-Gavrila et al. 2008; Sherlekar and Rikhy 2016; Dey and Rikhy 2020). Therefore, we further assessed the furrow length, polygon distribution, and cell shape index in DE-cad, Baz, and Pnut-depleted embryos. We found that *shg*^{i}-expressing embryos showed a significant decrease in furrow length in MP11, MP12, and MP13 as compared to control tGPH embryos. *baz*^{i}, and *pnut*^{i} expressing embryos showed a slight decrease in furrow length in MP11 and MP12 but not in MP13 (Fig. 4a and b, Supplementary Video 2–4). The furrow length in *shg*^{i} was approximately 6 in MP12 (approximately 34% decrease as compared to control which is approximately 9 μm) and approximately 9 in MP13 (approximately 30% decrease as compared to control which is approximately 13 μm). The furrow lengths in *baz*^{i} decreased to approximately 6 and *pnut*^{i} decreased to approximately 7 in the MP of NC12 (approximately 22% decrease as compared to control which is approximately 9 μm) (Fig. 4a and b). The furrow lengths in *baz*^{i} and *pnut*^{i} expressing embryos were longer in MP13 than MP12. The average furrow length reached approximately 11 μm and was not statistically different from control embryos (Fig. 4a and b). *shg*^{i} embryos showed shorter furrow lengths than the control in MP12 and MP13, and *baz* and *pnut* knockdowns especially in MP13 (Fig. 4a and b). Double depletion of Baz and Pnut also showed a decrease in furrow length similar to each of the single depletions (Supplementary Fig. 4d and e). We found that the rates of furrow ingression between Baz and Pnut depleted embryos were similar to controls (Supplementary Fig. 4c).

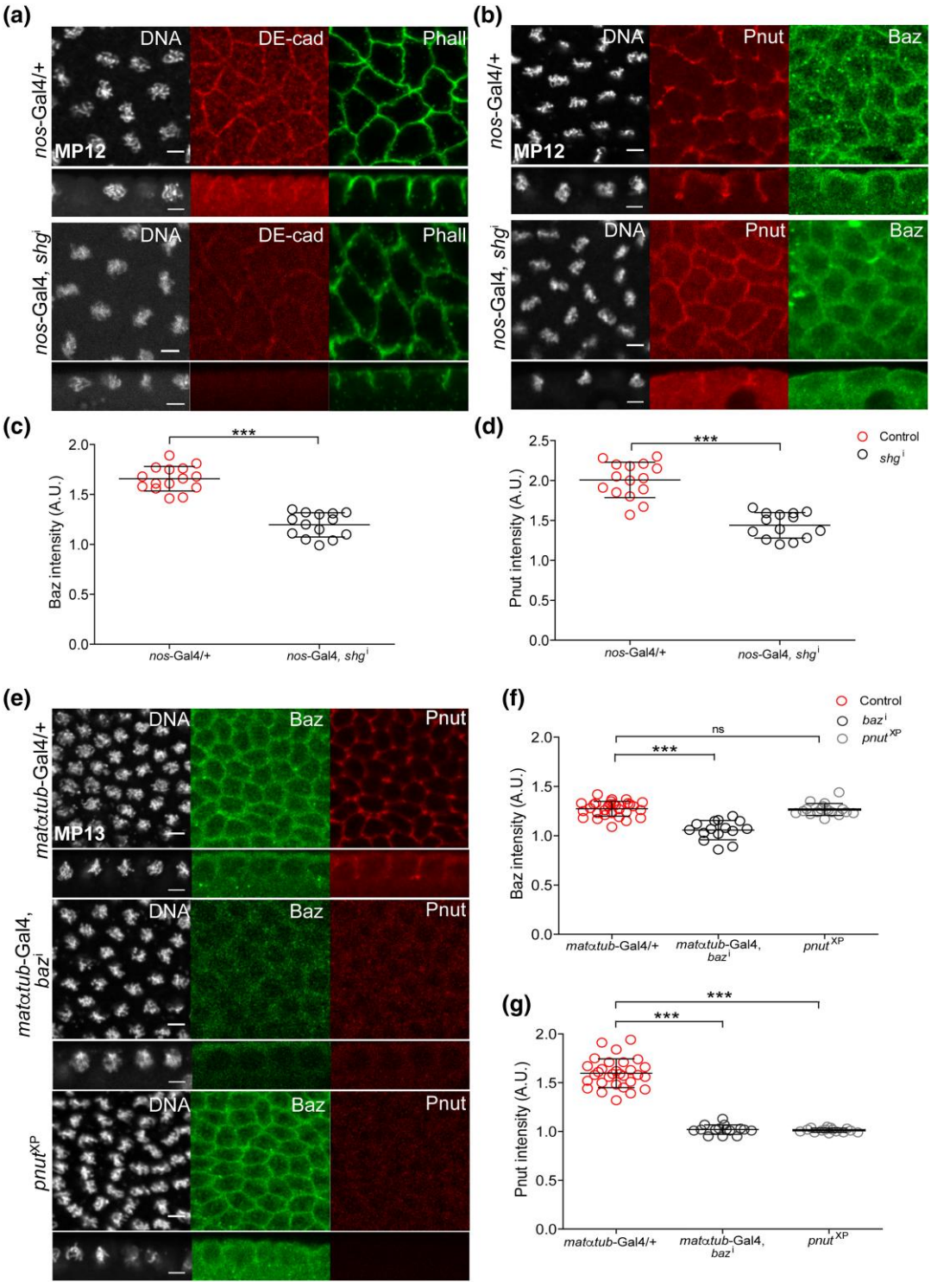

Fig. 3. DE-cad, Baz, and Pnut knockdown embryos show differential loss of polarity proteins at the MP furrow. a–d) DE-cad loss results in the lowering of DE-cad, Baz, and Pnut from the membrane. DE-cad is lowered in *shg*^{i} embryos. *nos*-Gal4/+ ($n = 10$) and *nos*-Gal4; *shg*^{i} (*shg*^{i}) (86% show loss of DE-cad, $n = 21$) embryos are co-stained with DE-cad and phalloidin in MP12 (a); Baz and Pnut in MP12 (b). Quantification of Baz and Pnut levels on the membrane in *shg*^{i} embryos using membrane to cytosol ratios from embryos in MP12 and MP13. Note the enrichment of Pnut at the vertices (white arrows). Baz (c) ($n = 5$ cells per embryo, 4 embryos) and Pnut (d) ($n = 4$–5 cells per embryo, 3 embryos) are both lowered in *shg*^{i} embryos (94% show loss of Baz and Pnut, $n = 16$). Scale bar: 5 µm. e–g) Baz loss results in a decrease of Pnut on the membrane. *matαtub*-Gal4/+ ($n = 20$), *matαtub*-Gal4; *baz*^{i} (*baz*^{i}), and *pnut*^{XP} (germline clone embryos, see Materials and methods) embryos co-stained with Baz and Pnut in MP13. *baz*^{i} shows a decrease in Baz and Pnut (100% loss of Baz and Pnut, $n = 20$) and *pnut*^{XP} shows the loss of Pnut (100% show loss of Pnut, $n = 17$) while Baz (100% embryos show no defect in Baz, $n = 11$) is unaffected (e). Graphs showing the quantification of Baz and Pnut intensities on the membrane using membrane to cytosol ratios in *baz*^{i} and *pnut*^{XP} embryos. Baz is lowered in *baz*^{i} ($n = 5$ cells per embryo, 4 embryos) but not in *pnut*^{XP} embryos ($n = 4$–5 cells per embryo, 4 embryos) (f). Pnut is lowered in both *baz*^{i} ($n = 4$–5 cells per embryo, 4 embryos) and *pnut*^{XP} embryos ($n = 5$ cells per embryo, 3 embryos) (g). Data is represented as mean ± SD, $^{*}P < 0.05$, $^{**}P < 0.01$, and $^{***}P < 0.001$, 2-tailed, unpaired Student's *t* test. Each point in the graph represents the membrane to cytosol ratio of the respective protein in syncytial cells across various embryos. Scale bar: 5 µm.

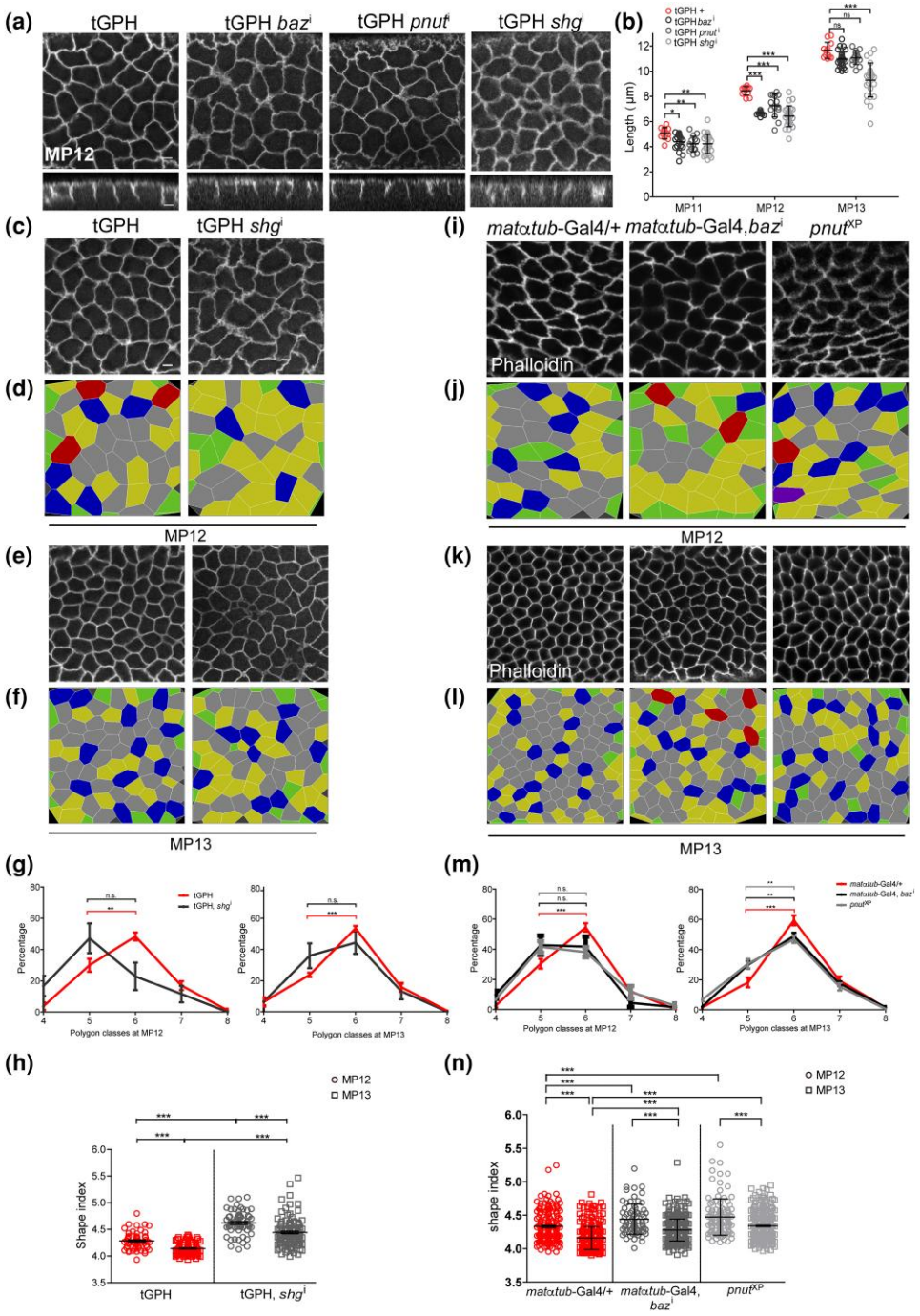

Fig. 4. DE-cad depletion shows a loss of hexagon dominance whereas. Baz and Pnut depletions show a delay in the onset of hexagon dominance. a and b) *baz*, *pnut*, *and shg* knockdown embryos show decreased furrow length. *atub84B*-tGPH (referred to as tGPH) grazing sections in MP12 for control, *matαtub*-Gal4; UAS-*baz*^{i} (*baz*^{i}), *matαtub*-Gal4, UAS-*pnut*^{i} (*pnut*^{i}), and *nos*-Gal4, *shg*^{i} (*shg*^{i}) at NC12 (a). Quantification of MP furrow lengths in tGPH/+, *baz*^{i}, *pnut*^{i}, and *shg*^{i} in NC11–13 ($n = 12$, 4 furrows each; 3 embryos) (c). Data is represented as mean ± SD, $^{*}P < 0.05$, $^{**}P < 0.01$, and $^{***}P < 0.001$, 2 tailed, unpaired Student's *t*-test. Scale bar: 5 µm. c–g) *shg*^{i} embryos show loss of hexagon dominance. tGPH/+ and tGPH; *matαtub*-Gal4, UAS-*shg*^{i} (*shg*^{i}) embryos in MP12–13 (c and e) along with the respective color-coded polygon renderings (d and f). Graph showing polygonal distribution in *shg*^{i} in MP12–13 (g) (n = approximately 120 syncytial cells, 20–30 cells/embryo; 4 embryos). Hexagon dominance is not seen in NC13. Pentagons and hexagons are compared in each cycle using the unpaired, 2 tailed, Student's *t*-test. Data is represented as mean ± SEM, $^{*}P < 0.05$, $^{**}P < 0.01$, and $^{***}P < 0.001$. Graph showing average shape index of all the cells in the field in control and *shg*^{i} embryos in MP12–13 (g) (n = approximately 120 syncytial cells, 20–30 cells/embryo; 4 embryos). The control tGPH cell shape index is repeated from Fig. 1e. Data is represented as mean ± SEM, $^{*}P < 0.05$, $^{**}P < 0.01$, and $^{***}P < 0.001$, 2-tailed, unpaired Student's *t*-test. The NC13 polygon distribution for the control is repeated from Fig. 1d. Scale bar: 5 µm. i–n) *baz*^{i} and *pnut*^{XP} embryos show a delay in the onset of hexagon dominance. Control (*matαtub*-Gal4/+), *matαtub*-Gal4, UAS-*baz*^{i} (*baz*^{i}) and *pnut*^{XP} (germ line clone) embryos stained with phalloidin in MP12–13 (i and k) along with the respective color-coded polygon renderings (j and l). Graph showing polygonal distribution in *baz*^{i} and *pnut*^{XP} in NC12–13 (m) (n = 60–80 syncytial cells, 20–30 cells/embryo; 4–5 embryos). Hexagon dominance in *baz*^{i} and *pnut*^{XP} recovers in NC13. Pentagons and hexagons are compared in each cycle using the 2 tailed, unpaired, Student's *t*-test. Data is represented as mean ± SEM, $^{*}P < 0.05$, $^{**}P < 0.01$, and $^{***}P < 0.001$. Graph showing average shape index of all the cells in the field in Control (+/+), *baz*^{i} and *pnut*^{XP} embryos in MP12–13 (n) (n = approximately 60–80 syncytial cells, 20–30 cells/embryo; 4–5 embryos) Data is represented as mean ± SEM, $^{*}P < 0.05$, $^{**}P < 0.01$, and $^{***}P < 0.001$, 2-tailed, unpaired Student's *t*-test. Scale bar: 5 µm.

We analyzed the polygonal distribution in DE-cad, Baz, and Pnut knockdown embryos in MP12 and MP13 by live imaging mutant embryos expressing tGPH, or with phalloidin staining. To assess the effect of DE-cad loss on polygonal distribution, we quantified the polygon types from the MP of *shg*^{i} live movies obtained with tGPH in the background. *shg*^{i} embryos showed pentagon dominance at MP12. The percentage of pentagons was significantly higher than hexagons in MP12 in *shg*^{i}, unlike control embryos which display hexagon dominance (Fig. 4c–e). *shg*^{i} expressing embryos showed a significant increase in pentagons in MP13 and there was no significant difference between pentagons and hexagons in MP13 as compared to hexagon dominance seen in control embryos (Fig. 4f–h). *shg*^{i} expressing embryos showed ruffled membranes as opposed to the taut and sharp membranes in the controls. The tGPH fluorescence at the furrow membrane was spread over a larger area as compared to control embryos (Supplementary Fig. 4a and b, Supplementary Video 4). Since control embryos showed hexagon dominance at MP and not at 6.5 μm in NC12 (Supplementary Fig. 1), the loss of hexagon dominance in *shg*^{i} expressing embryos is likely to be due to loss of adhesion thereby leading to decreased furrow stability and length in MP12 and MP13. The cell shape index also increased in *shg*^{i} expressing embryos (4.62 in MP12, 4.44 in MP13) as compared to controls (4.28 in MP12 and 4.14 in MP13) in MP12 and MP13 thereby indicating a shift to a more unstable or fluid network (Fig. 4h).

baz^{i} expressing embryos and *pnut*^{XP} germline clone embryos (Fig. 4i–o) stained with fluorescently coupled phalloidin showed a significant increase in the frequency of pentagons and loss of hexagon dominance in MP12 as compared to controls (Fig. 4i, j and m). However, the hexagon dominance was similar to controls in MP13 (Fig. 4k–m). The cell shape index was increased in Baz-depleted embryos as compared to controls (4.44 in MP12 and 4.28 in MP13 as compared to controls 4.33 in MP12 and 4.16 in MP13) (Fig. 4n). The cell shape index was increased in Pnut-depleted embryos as compared to controls (4.47 in MP12 and 4.34 in MP13) (Fig. 4n). Overexpression of the Baz oligomerization domain (BazΔ969-1464-GFP) that lowered Baz and depleted Pnut from the membrane also showed loss of hexagon dominance in MP12 and not in MP13 (Supplementary Fig. 5a–d). However, the cells were better organized as compared to *baz*^{i} and the cell shape index was almost similar to controls in these embryos suggesting that the expression of the oligomerization domain caused a less severe defect as compared to *baz*^{i} (Supplementary Fig. 5d). These data together showed that this decreased furrow length in MP did not support the organization of the PM in a hexagon dominated polygon array and in *baz*^{i} and *pnut*^{i} expressing embryos similar to controls at 6.5 μm (Supplementary Fig. 1). This is further corroborated by the observation that hexagon dominated polygon organization recovered in MP13 of *baz*^{i} and *pnut*^{i} expressing embryos, which also showed longer furrow lengths similar to control MP13. However, the cell shape index remained higher and the network remained more unstable in *baz*^{i} and *pnut*^{i} expressing embryos as compared to controls (Fig. 4k–n).

Therefore, our data shows that the decrease in furrow length seen upon loss of DE-cad, Baz, and Pnut is likely to cause a decrease in its stability as suggested by the increase in cell shape index, and loss of hexagon dominance in syncytial *Drosophila* embryos.

Recovery of hexagon dominance in Bazooka and Peanut mutant embryos occurs during syncytial cycle 13 with furrow extension

Hexagon dominance was seen in the syncytial *Drosophila* embryo on an increase in furrow length at MP in NC12 as well as at shorter furrow lengths of 6.5 μm in the prophase of NC13 (Supplementary Fig. 1b–d). Therefore, we analyzed whether hexagon dominance could also occur at shorter furrow lengths of 6.5 μm in NC13 in Baz and Pnut knockdown embryos. Since the predominant cell shapes in the syncytial embryos were hexagons and pentagons, we plotted the distribution of polygons and the ratio of pentagons to hexagons in controls, Baz, and Pnut depleted embryos, with respect to furrow length, from live movies of embryos expressing tGPH. For control embryos, we found that hexagon dominance was present when the polygonal array was established in NC13 at 6.5 μm in prophase and remained until MP (MP13). However, Baz and Pnut depleted embryos showed pentagon dominance at the furrow length of 6.5 μm in NC13, and hexagon dominance at the maximum furrow length in MP of NC13 (MP13) (Fig. 5a–e). The ratio of pentagons to hexagons increased in Baz and Pnut depleted embryos at 6.5 μm in NC13 and was significantly higher than controls (Fig. 5f) whereas at MP13, the ratio of pentagons to hexagons was not significantly different from controls (Fig. 5f). The cell shape index remained slightly higher than controls in both NC12 and NC13 at 6.5 μm and at MP (Fig. 5g). In summary, hexagon dominance occurred in NC13 in both Baz and Pnut knockdown embryos at longer furrow lengths in MP. It is possible that increased recruitment of polarity and adhesion complexes occurred at increased furrow length and this allowed the furrow to stabilize and get organized as a hexagon-dominant polygon array.

Bazooka and Peanut depleted embryos show an increase in DE-cadherin at the furrow

Furrow formation was affected in embryos depleted of DE-cad possibly due to lack of adhesion and stabilization of furrows. Unlike Baz- and Pnut-depleted embryos that show a delay in the onset of hexagon dominance, we found that loss of DE-cad led to the loss of hexagon dominance in both MP12 and MP13. We tested if DE-cad levels changed in Baz- and Pnut-depleted embryos. We hence imaged DE-cad distribution in live and fixed Baz- and Pnut-depleted embryos. DE-cad levels were estimated in Baz- and Pnut-depleted embryos by immunostaining for DE-cad using an antibody (Fig. 6) and expressing *ubi*-DE-cad-GFP in these embryos (Supplementary Video 5–7). Immunostaining with a DE-cad antibody showed that DE-cad levels increased on the furrow in MP12 and MP13 in Baz and Pnut depleted embryos as compared to controls (Fig. 6a–c). Baz and Pnut depleted embryos expressing DE-cad-GFP did not show a significant change in DE-cad-GFP fluorescence as compared to controls in MP12 (Supplementary Video 5–7). However, 50% of these embryos showed an increase in DE-cad-GFP fluorescence as compared to controls (Fig. 6d and f). DE-cad-GFP levels were significantly increased in MP13 in Baz and Pnut depleted embryos as to controls (Fig. 6e and f). In summary, we observe that DE-cad depletion leads to loss of hexagon dominance (Fig. 3) whereas Baz- and Pnut-depleted embryos showed hexagon dominance in MP13 at higher levels of DE-cad as compared to controls (Figs. 4 and 7). It is interesting to note that increased DE-cad in MP12 did not support hexagon dominance in the absence of Baz and Pnut.

Baz- and Pnut-depleted embryos show an increased accumulation of Dynamin and Rab5 at the furrow membrane

Polarity proteins are known to regulate endocytosis at the PM (Shivas et al. 2010). The levels of DE-cad at the PM will change based on the rates of endocytosis. DE-cad endocytosis increases in *Drosophila* tracheal tissues during active remodeling

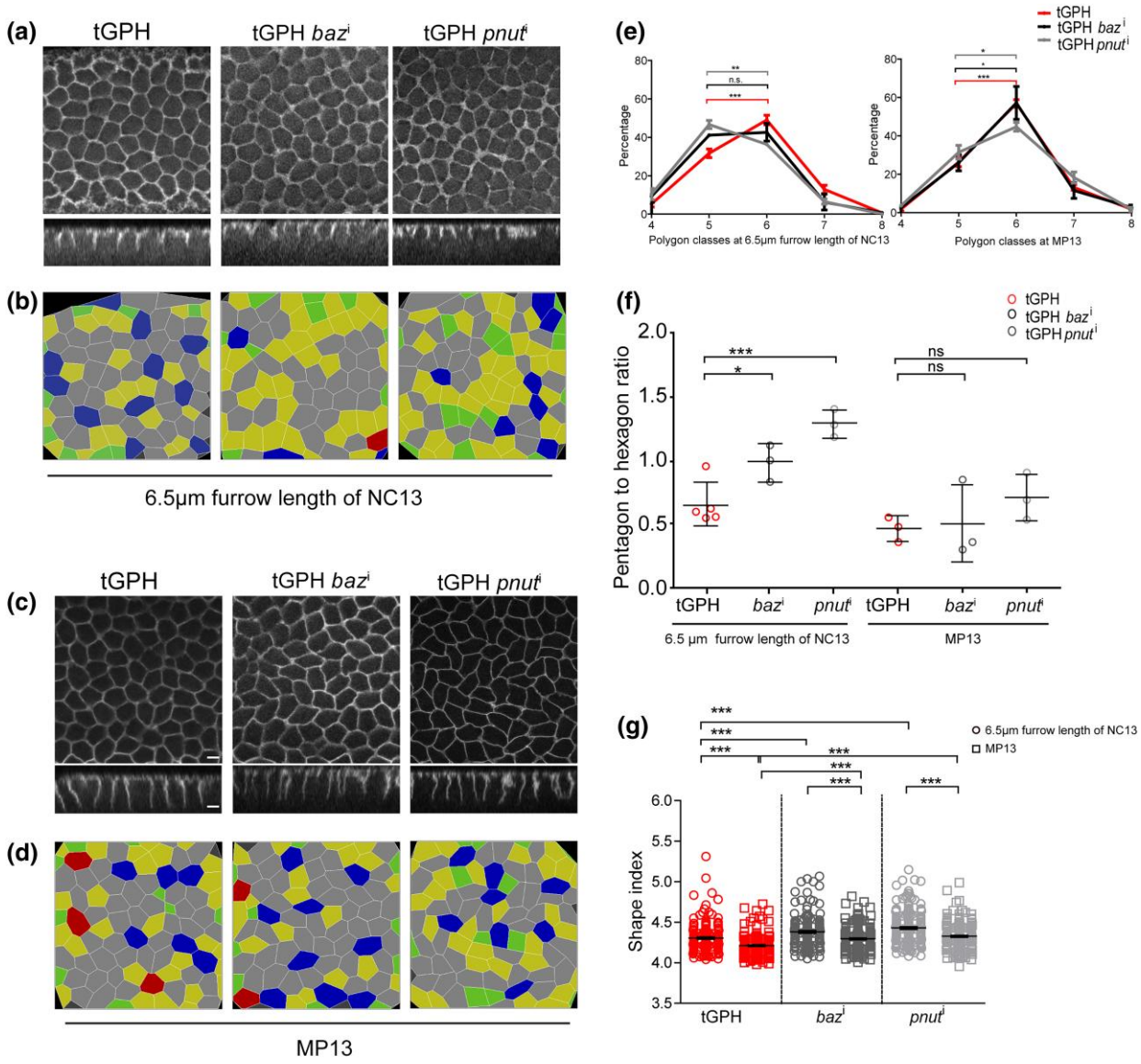

Fig. 5. Appearance of hexagon dominance in Baz and Pnut knockdowns occurs in MP of NC13. a and b) *matatub*-Gal4; *baz*^{i} (*baz*^{i}) and *matatub*-Gal4; *pnut*^{i} (*pnut*^{i}) embryos show loss of hexagon dominance at a shorter furrow length at NC13 when wildtype is already hexagon dominant. Grazing and sagittal sections of *atub84B*-tGPH (referred to as tGPH) expressing control, *baz*^{i} and *pnut*^{i} embryos at NC13 at a short furrow length of 6.5 µm (a) along with the respective color-coded polygon renderings (b). c and d) *baz*^{i} and *pnut*^{i} embryos show recovery of hexagon dominance at the maximum furrow length at MP13. Grazing and sagittal sections of tGPH expressing control, *baz*^{i} and *pnut*^{i} embryos at MP13 at maximum furrow length in MP (c) along with the respective color-coded polygon renderings (d). e–g) Baz and Pnut knockdowns show a length-dependent recovery of hexagon dominance at NC13. Graph showing the polygon distribution of control, *baz*^{i} and *pnut*^{i} embryos at NC13 at a short furrow length of 6.5 µm and at MP (e). Graph showing the pentagon to hexagon ratio of control, *baz*^{i} and *pnut*^{i} embryos at NC13 at a short furrow length of 6.5 µm and at MP (f). Data is represented as mean ± SEM, $^{*}P < 0.05$, $^{**}P < 0.01$, and $^{***}P < 0.001$, 2-tailed, unpaired Student's *t* test. Graph showing average shape index of all the cells in the field in control, *baz*^{i} and *pnut*^{i} embryos at NC13 at a short furrow length of 6.5 µm and at MP (g). Data is represented as mean ± SD, $^{*}P < 0.05$, $^{**}P < 0.01$, and $^{***}P < 0.001$, 2-tailed, unpaired Student's *t*-test. Scale bar = 5 µm.

(Shindo et al. 2008). DE-cad is present at higher levels at the PM in notum epithelial cells when endocytosis decreases in Par6 and aPKC mutants (Georgiou et al. 2008). Dynamin-mediated endocytosis is important for furrow extension in the syncytial blastoderm embryo (Rikhy et al. 2015). Increased accumulation of Dynamin at the furrow in temperature-sensitive mutants of Dynamin, *shibire*, shows decreased endocytosis and accumulation of DE-cad at the furrow (Rikhy et al. 2015). Since DE-cad increased in levels at the furrow in Baz- and Pnut-depleted embryos in MP12 and MP13, we assayed for distribution of Dynamin and early endosome protein Rab5 at the furrow in Baz- and Pnut-depleted embryos. We immunostained Baz and Pnut depleted embryos with Dynamin (Rikhy et al. 2015) and Rab5 (Tanaka et al. 2021) antibodies along with phalloidin and quantified the extent of change of fluorescence at the furrow as a ratio to the adjacent cytoplasm in MP12 and MP13. Dynamin is localized weakly at the furrow marked with phalloidin in control embryos in MP12 and MP13 (Fig. 7a and b). We found that there was an increase in Dynamin fluorescence at the furrow in the form of distinct punctae and in the cytoplasm in both Baz and Pnut depleted embryos (Fig. 7a and b). We specifically quantified the increase in Dynamin fluorescence at the furrow marked by phalloidin as a ratio to the cytoplasm and found that there is a significant increase at the furrow in MP12 and MP13 in Baz- and Pnut-depleted embryos (Fig. 7c).

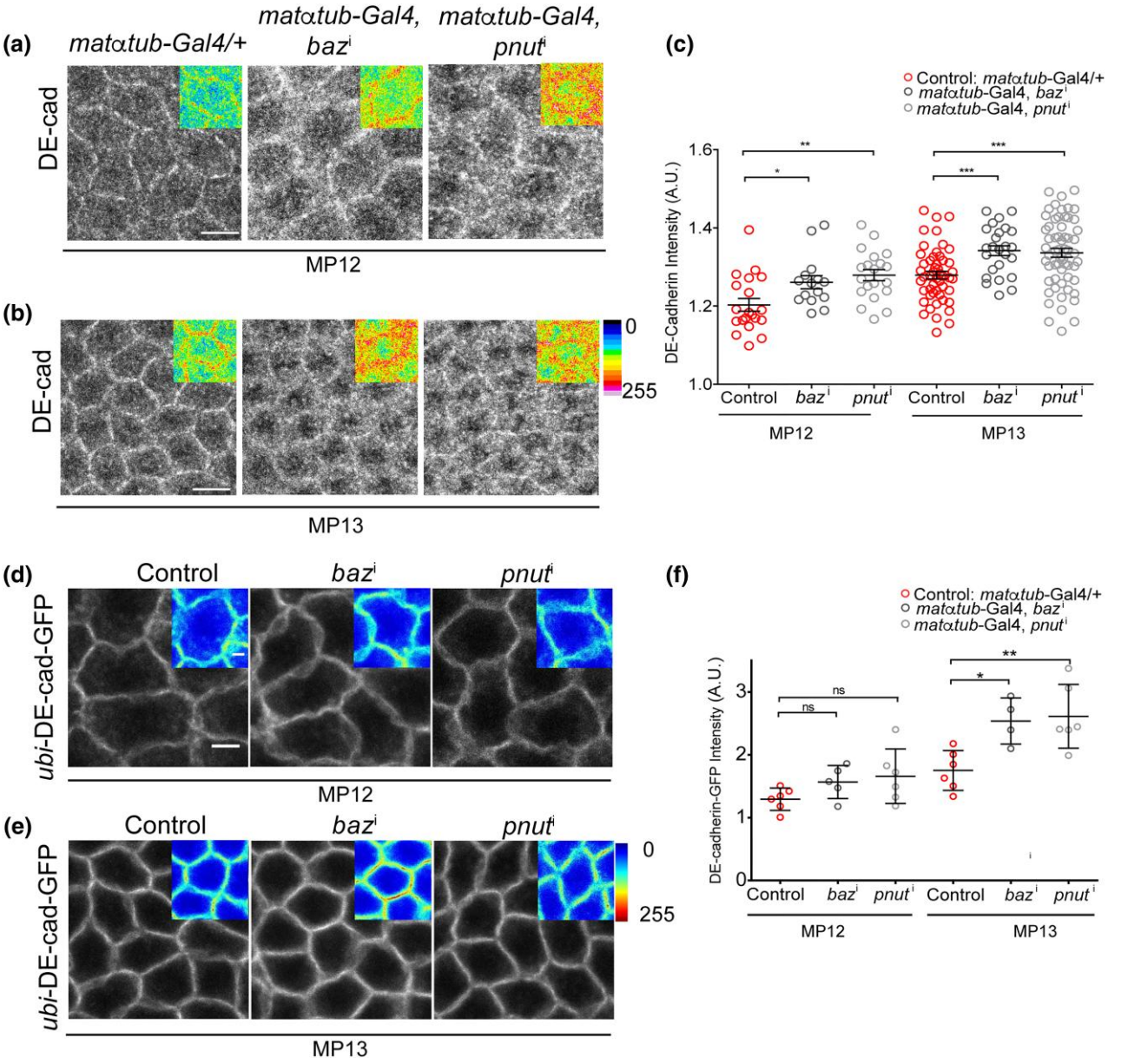

Fig. 6. DE-cad levels increase in Baz and Pnut knockdown embryos. a–c) Grazing sections of control, *matαtub*-Gal4; *baz*^{i} (*baz*^{i}) and *matαtub*-Gal4; *pnut*^{i} (*pnut*^{i}) stained with DE-cad in MP12–13 (a and b). Insets show zoomed in images. The 16 color rainbow scale from the imageJ is used to show fluorescent intensities. Graph showing quantification of the intensity of DE-cad on the membrane using membrane to cytosol ratios in *baz*^{i} (n = 15–25, 4–10 cells per embryo from MP12–13, 3–5 embryos) and *pnut*^{i} embryos (n = 20–60, 5–10 cells per embryo from MP12–13, 4–5 embryos) (c). DE-cad is increased in both *baz*^{i} and *pnut*^{i} embryos with higher significance value in MP13 than MP12. For MP12, DE-Cad accumulations are observed at approximately 2–2.4 microns of furrow length in both *baz*^{i} and *pnut*^{i} embryos. For MP13, DE-Cad accumulations are observed at around 2.4–4 microns of furrow length in both *baz*^{i} and *pnut*^{i} embryos. Data is represented as mean ± SD, *P < 0.05, **P < 0.01, and ***P < 0.001, 2-tailed, unpaired Student's t-test. Scale Bar = 10 µm. d–f) Grazing sections of *ubi*-DE-cad-GFP/+, *ubi*-DE-cad-GFP; *matαtub*-Gal4, UAS-*baz*^{i} (*baz*^{i}), and *ubi*-DE-cad-GFP; *matαtub*-Gal4, UAS-*pnut*^{i} (*pnut*^{i}) embryos in MP12–13 (d and e). Insets show zoomed in images. The 16 color rainbow scale from the imageJ is used to show fluorescent intensities. Graph showing quantification of normalized intensity of DE-cad on the membrane using membrane to cytosol ratios in *baz*^{i} and *pnut*^{i} embryos (n = 12–15, MP12–13, 5 cells per embryo, 5 embryos). DE-cad is increased in both *baz*^{i} and *pnut*^{i} embryos in MP13 (f). Data is represented as mean ± SD, *P < 0.05, **P < 0.01, and ***P < 0.001, 2-tailed, unpaired Student's t-test. Scale bar = 5 µm.

Rab5 fluorescence was observed in punctae and weakly at the furrow which is marked by phalloidin in control embryos in MP12 and MP13 (Fig. 7d and e). We found that there was an increased accumulation of Rab5 at the furrow in Baz- and Pnut-depleted embryos (Fig. 7d and e). We quantified the Rab5 fluorescence at the furrow in MP12 and MP13 embryos and found that there was a significant increase in accumulation at the furrow (Fig. 7f). This accumulation of Dynamin and Rab5 at the furrow implicates a decrease in endocytosis at the furrow PM in Baz and Pnut depleted embryos and this is likely to be the cause of the accumulation of DE-cad in NC12 and NC13. Future analysis of endocytic mutants will confirm whether loss of endocytosis, in general, leads to loss of furrow stability and hexagon-dominated polygon organization in the syncytial blastoderm *Drosophila* embryo.

In summary, we show that successive division cycles in the syncytial *Drosophila* blastoderm embryo show hexagon dominated PM organization, and a decrease in cell shape index accompanied by an increase in the concentration of polarity proteins at the

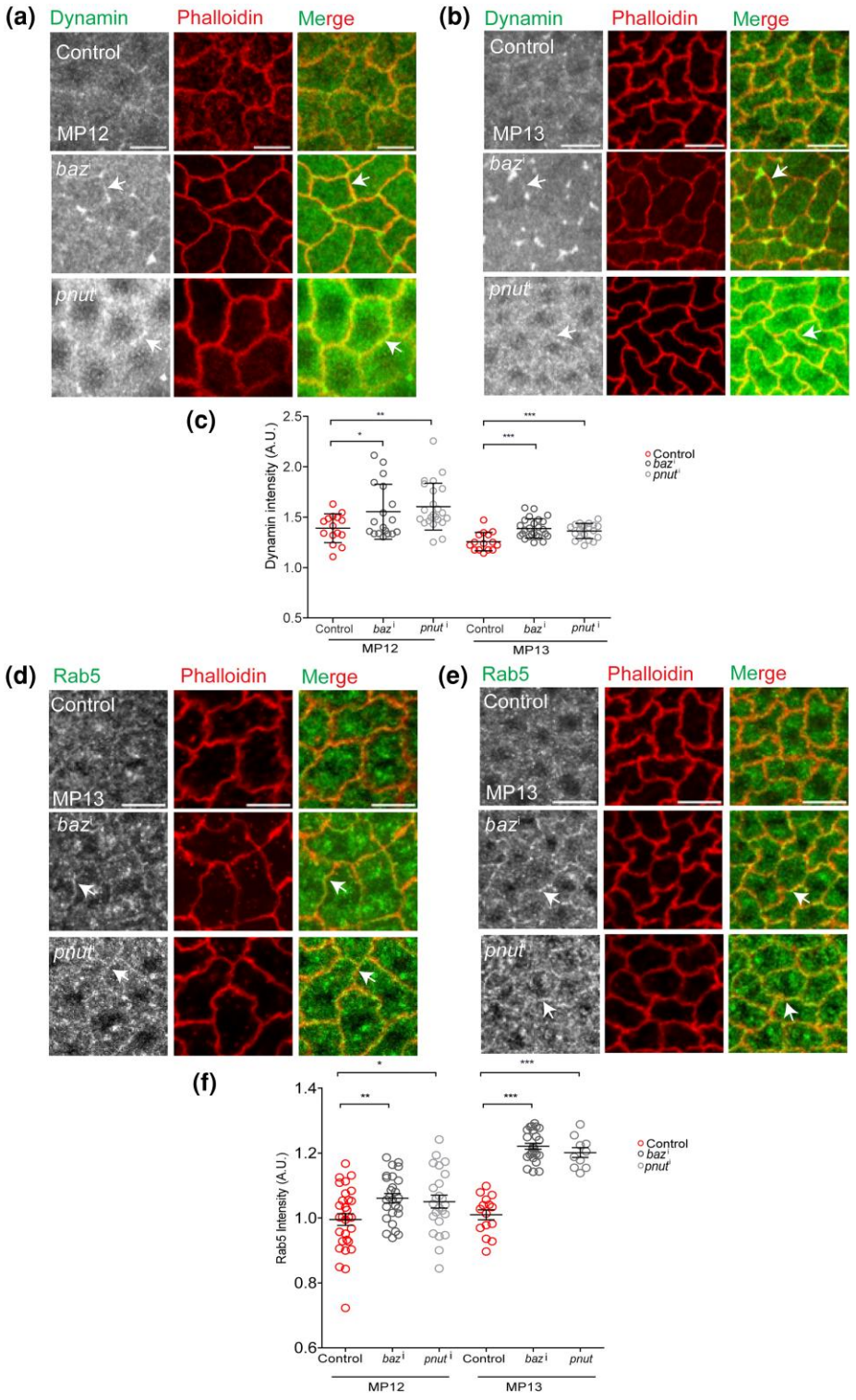

Fig. 7. Dynamin and Rab5 levels increase in Baz and Pnut knockdown embryos. a–c) Grazing sections of control (*matatub*-Gal4/+), *matatub*-Gal4, UAS-*baz*^{i} (*baz*^{i}) and *matatub*-Gal4, UAS-*pnut*^{i} (*pnut*^{i}) stained with Dynamin and Phalloidin in MP12 and MP13 (a and b). Graph showing quantification of fluorescence intensity of Dynamin on the membrane using membrane to cytosol ratios in *baz*^{i} ($n = 15–40$, 5 cells per embryo from MP12–13, 3–8 embryos) and *pnut*^{i} embryos ($n = 30–39$, 4–5 cells per embryo MP12–13, 6–8 embryos) (c). Dynamin is increased in both *baz*^{i} and *pnut*^{i} embryos with higher significance value in MP13 than MP12. For MP12, the image shown for Dynamin accumulations is at approximately 1.8–2.4 microns of furrow length in both *baz*^{i} and *pnut*^{i} embryos. For MP13, the image shown for Dynamin accumulation is at around 2.4–4 microns of furrow length in both *baz*^{i} and *pnut*^{i} embryos. Data is represented as mean ± SD, $^{*}P < 0.05$, $^{**}P < 0.01$, and $^{***}P < 0.001$, 2-tailed, unpaired Student's *t* test. Scale Bar = 10 µm. d–f) Grazing sections of control (+/+), *baz*^{i} and *pnut*^{i} stained with Rab5 in MP of MP12–13 (d and e). Graph showing quantification of intensity of Rab5 on the membrane using membrane to cytosol ratios in *baz*^{i} ($n = 25–26$, 4–5 cells per embryo from NC12–13, 5 embryos) and *pnut*^{i} embryos ($n = 10–25$, 5 cells per embryo from MP12–13, 2–5 embryos) (f). Rab5 is increased in both *baz*^{i} and *pnut*^{i} embryos in MP12 and MP13. For MP12, the image shown for Rab5 accumulation is at approximately 1.8–2.4 microns of furrow length in both *baz*^{i} and *pnut*^{i} embryos. For MP13, the image shown for Rab5 accumulations is at around 2.4–4 microns of furrow length in both *baz*^{i} and *pnut*^{i} embryos. Data is represented as mean ± SD, $^{*}P < 0.05$, $^{**}P < 0.01$, and $^{***}P < 0.001$, 2-tailed, unpaired Student's *t*-test. Scale Bar = 10 µm.

furrow. DE-cad regulates the formation of furrow, cell stability, and hexagon dominance. Baz and Pnut depleted embryos show hexagon dominance coincident with an increase in levels of DE-cad as compared to controls. It is likely that decreased cell shape index and delayed onset of hexagon-dominated polygon organization in Baz and Pnut depleted embryos occurs only when higher levels of DE-cad are obtained in MP13. These observations highlight an inter-regulation of polarity, adhesion, and endocytosis proteins in order to achieve appropriate stabilization of the furrow membrane to achieve a stable hexagon-dominated polygonal array in the syncytial *Drosophila* blastoderm embryo.

Discussion

In this study, we show that the formation of hexagon dominated PM organization in a relatively stable epithelial-like array occurs in the presence of a combination of adhesion and polarity proteins in the syncytial *Drosophila* blastoderm embryo from the MP stage of NC12. Pentagons and hexagons are equally likely in NC11 when edges first form and hexagons are present at a frequency of almost double the number of pentagons from the MP of NC12 up to NC13. Since the syncytial cycles do not have a complete basal domain, the lateral membrane, i.e. the pseudocleavage furrow, is sufficient to regulate the stability of the epithelial-like array showing hexagon dominance. There is a decrease in cell shape index across the syncytial cycle showing that increased crowding correlates with a more stable polygonal array. We have characterized the role of Baz, Pnut, and DE-cad proteins in the regulation of the lateral furrow length and polygon array distribution in the syncytial embryo. This analysis reveals furrow and polygon distribution phenotypes in 2 categories: (1) DE-cad depleted embryos have short furrows, loss of hexagon dominance, and an increase in cell shape index; (2) Baz- and Pnut-depleted embryos have slightly short furrows, delay in hexagon dominance and an increase in cell shape index. Even though the cell shape index is more than controls in DE-cad, Baz, and Pnut depleted embryos, there is a decrease from MP12 to MP13 showing that cell proliferation and associated changes in the PM give rise to a more stable network. Hexagon dominance appears in Baz and Pnut mutant embryos in NC13 with an increase in furrow lengths. This is coincident with an increase in DE-cad levels and accumulation of endocytic machinery at the furrow PM. These studies, therefore, reveal the requirement of stability of the furrow PM, by the combination of polarity and adhesion proteins, and further implicate endocytosis rates in the regulation of de novo hexagon dominant epithelial-like PM in the syncytial *Drosophila* embryo (Fig. 8). DE-cad function is more significant for furrow extension as compared to Baz and Pnut. Baz and Pnut are important for the stabilization of the furrow membrane to give rise to hexagonal dominant furrow membrane organization. Vertices mature and stabilize in NC12 with the accumulation of Baz at edges and Pnut at vertices. Baz presence on the furrow membrane is important for Pnut distribution.

DE-cad loss significantly decreased but did not completely abolish lateral furrows. If this is the major protein responsible for the stabilization of adhesion of furrow membranes of adjacent syncytial cells, we should have obtained a phenotype of complete loss of furrow but we only saw a reduction in furrow length. We argue that this could be due to the inability to deplete DE-cad completely with the RNAi strategy. Also, it could be due to the presence of other proteins that are responsible for keeping the furrow membrane adhered to each other. Other transmembrane proteins such as Crumbs, Neuroglian, and Neurexin are not present in syncytial embryos (Harris and Peifer 2004; Laprise et al. 2009). Future analysis of other cadherin-like adhesion molecules such as Echinoid may be useful in this direction (Wei et al. 2005).

We find that DE-cad levels regulate the stabilization of the furrow and the occurrence of hexagon dominance in the syncytial blastoderm embryo. DE-cad increases during the syncytial division cycles from MP11 to MP13 along with Baz and Pnut. An increase in DE-cad can also occur due to the loss of endocytosis and recycling in the *Drosophila* wing disc epithelium and blastoderm embryo (Classen et al. 2005; Rikhy et al. 2015; Iyer et al. 2019). We observed that Baz and Pnut depletion on the syncytial furrow led to an increase in DE-cad and accumulation of endocytic proteins at the furrow. This shows that Baz and Pnut depleted embryos show hexagon dominance at higher levels of DE-cad than controls. Since DE-cad depletion shows loss of hexagon dominance, this compensatory increase in DE-cad is likely to be responsible for the rescueof hexagon dominance in MP13 in

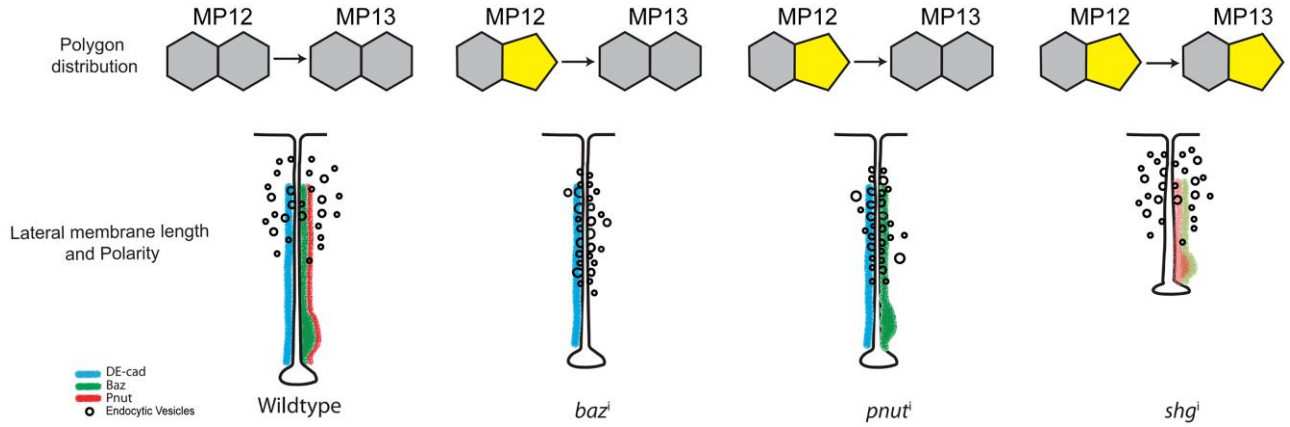

Fig. 8. Summary schematic showing the distribution of DE-cad, Baz and Pnut on the lateral furrow and polygon distribution in the *Drosophila* syncytial blastoderm embryo in NC13. Control embryos show hexagon dominance in MP12–13 with a significant amount of DE-cad, Baz, and Pnut on the lateral furrow. DE-cad undergoes endocytosis at the furrow membrane. Loss of Baz or Pnut results in a shorter furrow and delay in the onset of hexagon dominance while loss of DE-cad results in a shorter furrow along with a loss of hexagon dominance. Note the difference in the protein complex composition in the various mutants along with the possible accumulation of endocytic vesicles on the cell membrane. *baz*^{i} shows the loss of Baz and Pnut, while *pnut*^{i} shows loss of Pnut only. DE-cad is increased in *baz*^{i} and *pnut*^{i} in MP13 along with increased accumulation of endocytic machinery, which correlates with the recovery of hexagon dominance. *shg*^{i}, on the other hand, shows a decrease or mislocalization of DE-cad, Baz, and Pnut.

Baz- and Pnut-depleted embryos. Further elucidation of defects in proteins regulating membrane trafficking will also reveal the mechanisms by which endocytosis decreases in Baz and Pnut depleted embryos.

Baz and DE-cad play significant roles in being the primary molecules initiating the polarity program in different tissues. Baz initiates adherens junction polarity in *Drosophila* cellularization and gastrulation (Müller and Wieschaus 1996; Harris and Peifer 2004; Pilot et al. 2006) but is dispensable in follicle epithelial cells (Shahab et al. 2015). During mesoderm invagination, apical movement of DE-cad precedes the relocation of Baz, and thus, the asymmetry in DE-cad distribution here does not depend on Baz (Weng and Wieschaus 2017). This is similar to mammalian cells where E-cad is recruited to contact points before Baz (Coopman and Djiane 2016). This suggests that depending on the tissue type or developmental stage, the relative importance of Baz and E-cad in initiating polarity may change. We show that DE-cad is important for the distribution of both Baz and Pnut to the furrow. In the absence of identification of other adhesion proteins in the syncytial blastoderm embryo, we conclude that DE-cad assumes a significant role in furrow formation and stabilization in the *Drosophila* syncytial blastoderm embryo.

Asynchronous cell division in *Drosophila* wing disc epithelia is one of the mechanisms that give rise to a hexagon dominant and energy-minimized network (Gibson et al. 2006). It is interesting to note that synchronous divisions in the syncytial *Drosophila* blastoderm embryo also result in hexagon dominance in NC12. These observations are consistent with the presence of nuclei in a hexagon dominated polygonal organization in the syncytial *Drosophila* embryo (Kanesaki et al. 2011; Kaiser et al. 2018). Cytoskeletal dynamics coupled with polarity protein distribution favor the organization of this network.

A decreased number of edges in the polygonal array is a favorable state for cell neighbor exchanges and gives rise to a soft network (Farhadifar et al. 2007). The increase in pentagons in Baz and Pnut depleted embryos indicates a similar transition to a soft network possibly due to decreased stabilization of the furrow even in the presence of DE-cad and furrow length. The contacts in the Baz and Pnut mutant embryos are likely to facilitate neighbor exchanges. An increase in DE-cad on the furrow in MP13 in Baz and Pnut depleted embryos may allow for conversion back to hexagon-dominated state by formation and stabilization of one additional edge and vertex. Future analysis of change in furrow tension in various genetic backgrounds, along with mathematical modeling, will reveal the mechanisms that drive shape morphogenesis in *Drosophila* syncytial blastoderm embryos.

Data availability

The data underlying this article are available in the article and in its online Supplementary material.

Supplemental material available at GENETICS online.

Acknowledgments

We thank the R.R. lab members for their comments and discussion on the data in the manuscript. We thank the *Drosophila* and Microscopy facilities at IISER, Pune, India for help with stocks and microscopy for the experiments. We thank Benoit Aigouy for sharing the Packing analyzer software. We thank Andreas Wodarz (University of Goettingen, Germany) for the Bazooka antibody and Bazooka domain truncation stocks. We thank Manos Mavrakis (Institute Fresnel, Marseilles, France) for *peanut* mutant stocks and Sep1 and 2 antibodies. Stocks obtained from the Bloomington *Drosophila* Stock Center (NIH P40OD018537) were used in this study. R.R. thanks the Wellcome Trust DBT India Alliance Senior Fellowship IA/S/22/1/506232 for support to the lab.

Funding

R.R. thanks the Department of Biotechnology, Ministry of Science and Technology, India for funding BT/PR17317/BRB/10/1521/2016 to this project.

Conflicts of interest

The author(s) declare no conflict of interest.

Literature cited

Aegerter-Wilmsen T, Smith AC, Christen AJ, Aegerter CM, Hafen E, Basler K. 2010. Exploring the effects of mechanical feedback on epithelial topology. Development. 137(3):499–506. doi:10.1242/dev.041731.

Benton R, St Johnston D. 2003. Drosophila PAR-1 and 14-3-3 inhibit Bazooka/PAR-3 to establish complementary cortical domains in polarized cells. Cell. 115(6):691–704. doi:10.1016/S0092-8674(03)00938-3.

Bi D, Lopez JH, Schwarz JM, Manning ML. 2015. A density-independent rigidity transition in biological tissues. Nat Phys. 11(12):1074–1079. doi:10.1038/nphys3471.

Bilder D, Li M, Perrimon N. 2000. Cooperative regulation of cell polarity and growth by Drosophila tumor suppressors. Science. 289(5476):113–116. doi:10.1126/science.289.5476.113.

Britton JS, Lockwood WK, Li L, Cohen SM, Edgar BA. 2002. Drosophila's insulin/PI3-kinase pathway coordinates cellular metabolism with nutritional conditions. Dev Cell. 2(2):239–249. doi:10.1016/S1534-5807(02)00117-X.

Classen A-K, Anderson KI, Marois E, Eaton S. 2005. Hexagonal packing of Drosophila wing epithelial cells by the planar cell polarity pathway. Dev Cell. 9(6):805–817. doi:10.1016/j.devcel.2005.10.016.

Coopman P, Djiane A. 2016. Adherens Junction and E-cadherin complex regulation by epithelial polarity. Cell Mol Life Sci. 73(18):3535–3553. doi:10.1007/s00018-016-2260-8.

Dey B, Rikhy R. 2020. DE-cadherin and Myosin II balance regulates furrow length for onset of polygon shape in syncytial Drosophila embryos. J Cell Sci. 133(10):jcs240168. doi:10.1242/jcs.240168.

Farhadifar R, Röper J-C, Aigouy B, Eaton S, Jülicher F. 2007. The influence of cell mechanics, cell-cell interactions, and proliferation on epithelial packing. Curr Biol. 17(24):2095–2104. doi:10.1016/j.cub.2007.11.049.

Foe VE, Alberts BM. 1983. Studies of nuclear and cytoplasmic behaviour during the five mitotic cycles that precede gastrulation in Drosophila embryogenesis. J Cell Sci. 61(1):31–70. doi:10.1242/jcs.61.1.31.

Foe VE, Field CM, Odell GM. 2000. Microtubules and mitotic cycle phase modulate spatiotemporal distributions of F-actin and myosin II in Drosophila syncytial blastoderm embryos. Development. 127(9):1767–1787. doi:10.1242/dev.127.9.1767.

Georgiou M, Marinari E, Burden J, Baum B. 2008. Cdc42, Par6, and aPKC regulate Arp2/3-mediated endocytosis to control local adherens junction stability. Curr Biol. 18(21):1631–1638. doi:10.1016/j.cub.2008.09.029.

Gibson MC, Patel AB, Nagpal R, Perrimon N. 2006. The emergence of geometric order in proliferating metazoan epithelia. Nature. 442(7106):1038–1041. doi:10.1038/nature05014.

Gramates LS, Agapite J, Attrill H, Calvi BR, Crosby MA, dos Santos G, Goodman JL, Goutte-Gattat D, Jenkins VK, Kaufman T, *et al.* 2022. Flybase: a guided tour of highlighted features. Genetics. 220(4): iyac035. doi:10.1093/genetics/iyac035.

Guillot C, Lecuit T. 2013. Mechanics of epithelial tissue homeostasis and morphogenesis. Science. 340(6137):1185–1189. doi:10.1126/science.1235249.

Harris TJC, Peifer M. 2004. Adherens junction-dependent and -independent steps in the establishment of epithelial cell polarity in Drosophila. J Cell Biol. 167(1):135–147. doi:10.1083/jcb.200406024.

Hayashi T, Carthew RW. 2004. Surface mechanics mediate pattern formation in the developing retina. Nature. 431(7009):647–652. doi:10.1038/nature02952.

Holly RM, Mavor LM, Zuo Z, Blankenship JT. 2015. A rapid, membrane-dependent pathway directs furrow formation through RalA in the early Drosophila embryo. Development. 142(13):2316–2328. doi:10.1242/dev.120998.

Huang J, Zhou W, Dong W, Watson AM, Hong Y. 2009. From the Cover: directed, efficient, and versatile modifications of the Drosophila genome by genomic engineering. Proc Natl Acad Sci U S A. 106(20):8284–8289. doi:10.1073/pnas.0900641106.

Ikenouchi J, Furuse M, Furuse K, Sasaki H, Tsukita S, Tsukita S. 2005. Tricellulin constitutes a novel barrier at tricellular contacts of epithelial cells. J Cell Biol. 171(6):939–945. doi:10.1083/jcb.200510043.

Iyer KV, Piscitello-Gómez R, Paijmans J, Jülicher F, Eaton S. 2019. Epithelial viscoelasticity is regulated by mechanosensitive E-cadherin turnover. Curr Biol. 29(4):578–591.e5. doi:10.1016/j.cub.2019.01.021.

Kaiser F, Lv Z, Marques Rodrigues D, Rosenbaum J, Aspelmeier T, Großhans J, Alim K. 2018. Mechanical model of nuclei ordering in Drosophila embryos reveals dilution of stochastic forces. Biophys J. 114(7):1730–1740. doi:10.1016/j.bpj.2018.02.018.

Kalaji R, Wheeler AP, Erasmus JC, Lee SY, Endres RG, Cramer LP, Braga VM. 2012. ROCK1 And ROCK2 regulate epithelial polarisation and geometric cell shape. Biol Cell. 104(8):435–451. doi:10.1111/boc.201100093.

Kanesaki T, Edwards CM, Schwarz US, Grosshans J. 2011. Dynamic ordering of nuclei in syncytial embryos: a quantitative analysis of the role of cytoskeletal networks. Integr Biol (Camb). 3(11): 1112–1119. doi:10.1039/c1ib00059d.

Krahn MP, Bückers J, Kastrup L, Wodarz A. 2010. Formation of a Bazooka-Stardust complex is essential for plasma membrane polarity in epithelia. J Cell Biol. 190(5):751–760. doi:10.1083/jcb.201006029.

Laprise P, Lau KM, Harris KP, Silva-Gagliardi NF, Paul SM, Beronja S, Beitel GJ, McGlade CJ, Tepass U. 2009. Yurt, Coracle, Neurexin IV and the Na+, K+-ATPase form a novel group of epithelial polarity proteins. Nature. 459(7250):1141–1145. doi:10.1038/nature08067.

Laprise P, Tepass U. 2011. Novel insights into epithelial polarity proteins in Drosophila. Trends Cell Biol. 21(7):401–408. doi:10.1016/j.tcb.2011.03.005.

Letizia A, Ricardo S, Moussian B, Martín N, Llimargas M. 2013. A functional role of the extracellular domain of Crumbs in cell architecture and apicobasal polarity. J Cell Sci. 126(Pt 10):2157–2163. doi:10.1242/jcs.122382.

Lv Z, Rosenbaum J, Mohr S, Zhang X, Kong D, Preiß H, Kruss S, Alim K, Aspelmeier T, Großhans J. 2020. The emergent yo-yo movement of nuclei driven by cytoskeletal remodeling in pseudo-synchronous mitotic cycles. Curr Biol. 30(13):2564–2573.e5. doi:10.1016/j.cub.2020.04.078.

Mavrakis M, Rikhy R, Lilly M, Lippincott-Schwartz J. 2008. Fluorescence imaging techniques for studying Drosophila embryo development. Curr Protoc Cell Biol. Chapter 4:Unit 4.18. doi:10.1002/0471143030.cb0418s39.

Mavrakis M, Rikhy R, Lippincott-Schwartz J. 2009. Plasma membrane polarity and compartmentalization are established before cellularization in the fly embryo. Dev Cell. 16(1):93–104. doi:10.1016/j.devcel.2008.11.003.

Miller KG, Karr TL, Kellogg DR, Mohr IJ, Walter M, Alberts BM. 1985. Studies on the cytoplasmic organization of early Drosophila embryos. Cold Spring Harb Symp Quant Biol. 50:79–90. doi:10.1101/SQB.1985.050.01.012.

Müller HA, Wieschaus E. 1996. Armadillo, bazooka, and stardust are critical for early stages in formation of the zonula adherens and maintenance of the polarized blastoderm epithelium in Drosophila. J Cell Biol. 134(1):149–163. doi:10.1083/jcb.134.1.149.

Nance J. 2014. Getting to know your neighbor: cell polarization in early embryos. J Cell Biol. 206(7):823–832. doi:10.1083/jcb.201407064.

Neufeld TP, Rubin GM. 1994. The Drosophila Peanut gene is required for cytokinesis and encodes a protein similar to yeast putative bud neck filament proteins. Cell. 77(3):371–379. doi:10.1016/0092-8674(94)90152-X.

Park JA, Kim JH, Bi D, Mitchel JA, Qazvini NT, Tantisira K, Park CY, McGill M, Kim S-H, Gweon B, *et al.* 2015. Unjamming and cell shape in the asthmatic airway epithelium. Nat Mater. 14(10): 1040–1048. doi:10.1038/nmat4357.

Pesacreta TC, Byers TJ, Dubreuil R, Kiehart DP, Branton D. 1989. Drosophila Spectrin: the membrane skeleton during embryogenesis. J Cell Biol. 108(5):1697–1709. doi:10.1083/jcb.108.5.1697.

Pilot F, Philippe J-M, Lemmers C, Lecuit T. 2006. Spatial control of actin organization at adherens junctions by a synaptotagmin-like protein Btsz. Nature. 442(7102):580–584. doi:10.1038/nature04935.

Rikhy R, Mavrakis M, Lippincott-Schwartz J. 2015. Dynamin regulates metaphase furrow formation and plasma membrane compartmentalization in the syncytial Drosophila embryo. Biol Open. 4(3):301–311. doi:10.1242/bio.20149936.

Sánchez-Gutiérrez D, Sáez A, Pascual A, Escudero LM. 2013. Topological progression in proliferating epithelia is driven by a unique variation in polygon distribution. PLoS One. 8(11):e79227. doi:10.1371/journal.pone.0079227.

Schmidt A, Grosshans J. 2018. Dynamics of cortical domains in early Drosophila development. J Cell Sci. 131(7):jcs212795. doi:10.1242/jcs.212795.

Schmidt A, Lv Z, Großhans J. 2018. ELMO and Sponge specify subapical restriction of Canoe and formation of the subapical domain in early Drosophila embryos. Development. 145(2):dev157909. doi:10.1242/dev.157909.

Schneider CA, Rasband WS, Eliceiri KW. 2012. NIH Image to ImageJ: 25 years of image analysis. Nat Methods. 9(7):671–675. doi:10.1038/nmeth.2089.

Schulte J, Tepass U, Auld VJ. 2003. Gliotactin, a novel marker of tricellular junctions, is necessary for septate junction development in Drosophila. J Cell Biol. 161(5):991–1000. doi:10.1083/jcb.200303192.

Shahab J, Tiwari MD, Honemann-Capito M, Krahn MP, Wodarz A. 2015. Bazooka/PAR3 is dispensable for polarity in Drosophila follicular epithelial cells. Biol Open. 4(4):528–541. doi:10.1242/bio.201410934.

Sherlekar A, Mundhe G, Richa P, Dey B, Sharma S, Rikhy R. 2020. F-BAR domain protein Syndapin regulates actomyosin dynamics during apical cap remodeling in syncytial Drosophila embryos. J Cell Sci. 133(10):jcs235846. doi:10.1242/jcs.235846.

Sherlekar A, Rikhy R. 2016. Syndapin promotes pseudocleavage furrow formation by actin organization in the syncytial Drosophila embryo. Mol Biol Cell. 27(13):2064–2079. doi:10.1091/mbc.E15-09-0656.

Shindo M, Wada H, Kaido M, Tateno M, Aigaki T, Tsuda L, Hayashi S. 2008. Dual function of Src in the maintenance of adherens junctions during tracheal epithelial morphogenesis. Development. 135(7):1355–1364. doi:10.1242/dev.015982.

Shivas JM, Morrison HA, Bilder D, Skop AR. 2010. Polarity and endocytosis: reciprocal regulation. Trends Cell Biol. 20(8):445–452. doi:10.1016/j.tcb.2010.04.003.

Silverman-Gavrila RV, Hales KG, Wilde A. 2008. Anillin-mediated targeting of Peanut to pseudocleavage furrows is regulated by the GTPase Ran. Mol Biol Cell. 19(9):3735–3744. doi:10.1091/mbc.e08-01-0049.

Silverman-Gavrila RV, Silverman-Gavrila LB. 2008. Septins: new microtubule interacting partners. ScientificWorldJournal. 8: 611–620. doi:10.1100/tsw.2008.87.

Stevenson V, Hudson A, Cooley L, Theurkauf WE. 2002. Arp2/3-dependent pseudocleavage [correction of psuedocleavage] furrow assembly in syncytial Drosophila embryos. Curr Biol. 12(9): 705–711. doi:10.1016/S0960-9822(02)00807-2.

Sugimura K, Ishihara S. 2013. The mechanical anisotropy in a tissue promotes ordering in hexagonal cell packing. Development. 140(19):4091–4101. doi:10.1242/dev.094060.

Tanaka T, Tani N, Nakamura A. 2021. Receptor-mediated yolk uptake is required for oskar mRNA localization and cortical anchorage of germ plasm components in the Drosophila oocyte. PLoS Biol. 19(4):e3001183. doi:10.1371/journal.pbio.3001183.

Thomas CM, Williams JA. 1999. Dynamic rearrangement of the spectrin membrane skeleton during the generation of epithelial polarity in Drosophila. J Cell Sci. 112(Pt 17):2843–2852. doi:10.1242/jcs.112.17.2843.

Vishwakarma M, Thurakkal B, Spatz JP, Das T. 2020. Dynamic heterogeneity influences the leader–follower dynamics during epithelial wound closure. Philos Trans R Soc Lond B Biol Sci. 375(1807):20190391. doi:10.1098/rstb.2019.0391.

Wang X, Merkel M, Sutter LB, Erdemci-Tandogan G, Manning ML, Kasza KE. 2020. Anisotropy links cell shapes to tissue flow during convergent extension. Proc Natl Acad Sci U S A. 117(24):13541–13551. doi:10.1073/pnas.1916418117.

Wei S-Y, Escudero LM, Yu F, Chang L-H, Chen L-Y, Ho Y-H, Lin C-M, Chou C-S, Chia W, Modolell J, *et al.* 2005. Echinoid is a component of adherens junctions that cooperates with DE-cadherin to mediate cell adhesion. Dev Cell. 8(4):493–504. doi:10.1016/j.devcel.2005.03.015.

Weng M, Wieschaus E. 2017. Polarity protein Par3/Bazooka follows myosin-dependent junction repositioning. Dev Biol. 422(2): 125–134. doi:10.1016/j.ydbio.2017.01.001.

Wodarz A, Ramrath A, Kuchinke U, Knust E. 1999. Bazooka provides an apical cue for Inscuteable localization in Drosophila neuroblasts. Nature. 402(6761):544–547. doi:10.1038/990128.

Xie Y, Blankenship JT. 2018. Differentially-dimensioned furrow formation by zygotic gene expression and the MBT. PLoS Genet. 14(1):e1007174. doi:10.1371/journal.pgen.1007174.

Zallen JA, Cohen Y, Hudson AM, Cooley L, Wieschaus E, Schejter ED. 2002. SCAR Is a primary regulator of Arp2/3-dependent morphological events in Drosophila. J Cell Biol. 156(4):689–701. doi:10.1083/jcb.200109057.

Editor: D. Andrew